




# Mitochondria, ER, and nuclear membrane defects reveal early mechanisms for upper motor neuron vulnerability with respect to TDP-43 pathology

Mukesh Gautam<sup>1,2</sup> · Javier H. Jara<sup>1,2</sup> · Nuran Kocak<sup>1,2</sup> · Lauren E. Rylaarsdam<sup>1</sup> · Ki Dong Kim<sup>1</sup> · Eileen H. Bigio<sup>3,4</sup> · P. Hande Özdinler<sup>1,2,4,5</sup> 

Received: 1 October 2018 / Revised: 9 November 2018 / Accepted: 10 November 2018

© Springer-Verlag GmbH Germany, part of Springer Nature 2018

## Abstract

Insoluble aggregates containing TDP-43 are widely observed in the diseased brain, and defined as “TDP-43 pathology” in a spectrum of neurodegenerative diseases, such as amyotrophic lateral sclerosis (ALS), Alzheimer’s disease and ALS with frontotemporal dementia. Here we report that Betz cells of patients with TDP-43 pathology display a distinct set of intracellular defects especially at the site of nuclear membrane, mitochondria and endoplasmic reticulum (ER). Numerous TDP-43 mouse models have been generated to discern the cellular and molecular basis of the disease, but mechanisms of neuronal vulnerability remain unknown. In an effort to define the underlying causes of corticospinal motor neuron (CSMN) degeneration, we generated and characterized a novel CSMN reporter line with TDP-43 pathology, the prp-TDP-43<sup>A315T</sup>-UeGFP mice. We find that TDP-43 pathology related intracellular problems emerge very early in the disease. The Betz cells in humans and CSMN in mice both have impaired mitochondria, and display nuclear membrane and ER defects with respect to TDP-43 pathology.

**Keywords** ALS · CSMN · Betz cells · Selective vulnerability

**Electronic supplementary material** The online version of this article (<https://doi.org/10.1007/s00401-018-1934-8>) contains supplementary material, which is available to authorized users.

✉ P. Hande Özdinler  
ozdinler@northwestern.edu

<sup>1</sup> Davee Department of Neurology and Clinical Neurological Sciences, Northwestern University Feinberg School of Medicine, Chicago, IL, USA

<sup>2</sup> Les Turner ALS Research and Patient Center, Chicago, IL, USA

<sup>3</sup> Department of Pathology, Northwestern University, Chicago, IL, USA

<sup>4</sup> Cognitive Neurology and Alzheimer’s Disease Center, Northwestern University Feinberg School of Medicine, Chicago, IL, USA

<sup>5</sup> Robert H. Lurie Comprehensive Cancer Center, Northwestern University, 303 E Chicago Ave., Ward 10-015, Chicago, IL 60611, USA

## Introduction

Trans-activation response DNA-binding protein of 43 kDa (TDP-43) is a 414-amino acid heterogeneous nuclear ribonucleoprotein (hnRNP), with two highly conserved RNA recognition motifs, a nuclear localization signal, and a glycine-rich region mediating most of its protein–protein interactions [8]. The involvement of TDP-43 was first reported in nuclear RNA transcription, mRNA stability regulation and modulation of mRNA splicing [9, 10, 12]. In addition, TDP-43’s role in a wide variety of cellular events, such as nucleocytoplasmic transport [51], mitochondrial stability [31], and autophagy pathways [6, 67], are beginning to emerge.

The discovery of TDP-43 aggregates, or aggregates that contained phosphorylated TDP-43 protein in a vast majority of neurodegenerative cases, defined the term “TDP-43 pathology” [38, 40]. In addition, diffusion and accumulation of TDP-43 in the cytoplasm was considered part of TDP-43 toxicity in neurons [38, 44]. Identification of about 60 different mutations within the *TARDBP* gene [8]—which codes for TDP-43 protein—in amyotrophic lateral sclerosis (ALS) patients further reinforced the importance and

relevance of TDP-43 protein with respect to motor neuron health and function. TDP-43-positive (TDP-43<sup>+</sup>) aggregates were detected in the brains of patients with frontotemporal lobar degeneration (FTLD) and ALS with FTLD [44]. Today, about 97% of ALS patients are found to have TDP-43 accumulations, one of the largest common pathology that is observed in a broad spectrum of ALS patients, including sporadic ALS (sALS), familial ALS (fALS, with the exception of SOD1-related fALS) and ALS with FTLD [38].

Since ALS is a disease of both upper and lower motor neurons, it is important to investigate the cortical component with respect to disease pathology. TDP-43<sup>+</sup> inclusions are indeed detected in the motor cortex of ALS patients [14], and these can be extracellular dystrophic neurites (DNs), as well as neuronal cytoplasmic inclusions (NCIs) and glial cytoplasmic inclusions (GCIs), representing a broad spectrum of protein aggregation defects, affecting a large region within the motor cortex and CNS. Interestingly, TDP-43<sup>+</sup> accumulations are detected in cell populations that are not affected in ALS, but some of the Betz cells, which degenerate in ALS, were devoid of TDP-43<sup>+</sup> accumulations [7], suggesting a lack of direct correlation between the presence of accumulations and cell death, but rather a broader implication for neuronal degeneration. Building evidence also argues against the hypothesis that only the cells or neurons that include TDP-43<sup>+</sup> accumulations undergo degeneration [2]. Therefore, we were compelled to investigate Betz cells of ALS patients with a broad spectrum of TDP-43 pathology detected in their motor cortex (Table 1).

Numerous mouse models were generated to reveal the extent of neuropathology and to bring a mechanistic insight

into neuronal vulnerability and degeneration with respect to *TARDBP* mutations detected in ALS patients. The relevance of such endeavor is justified by the acceptance of TDP-43 as the most commonly observed pathology in ALS and by the multiple unanswered questions to the broad role of TDP-43 in the motor cortex pathology. Of more concern to us, it is to investigate the reasons that lead to upper motor neuron vulnerability in the presence of *TARDBP* mutations. The prp-TDP-43<sup>A315T</sup> mouse model is a useful TDP-43 model because it mimics many aspects of the disease [72]. We, therefore, generated a CSMN reporter line of prp-TDP-43<sup>A315T</sup> mice to visualize and study the intracellular defects that occur in CSMN with respect to TDP-43 at different stages of disease progression.

Selective neuronal vulnerability and progressive degeneration of distinct neuronal populations distinguish neurodegenerative diseases from each other. TDP-43 pathology emerges as a converging path, and it is also observed in a subset of Alzheimer's [1], Parkinson's [43] and ALS/FTLD patients [44]. It is thus even more important to determine the intracellular defects that occur with respect to TDP-43 pathology, as they may reveal the common underlying causes of neuronal vulnerability. We studied upper motor neurons and investigated the CSMN in diseased mice due to mutation in the gene that codes for TDP-43 and Betz cells of ALS patients with confirmed TDP-43 pathology. Focusing our attention on the neurons that display vulnerability and undergo progressive degeneration helped us overcome the species barrier and uncovered the common cellular defects especially at the nuclear membrane, mitochondrial inner membrane, and endoplasmic reticulum (ER), suggesting new

**Table 1** Patient information

| Gender | Age of onset | Age of death | Clinical diagnosis and pathological assessment | TDP+NCIs | TDP+GCIs | TDP+DNs | PMI/h |
|--------|--------------|--------------|------------------------------------------------|----------|----------|---------|-------|
| M      | 59           | 61           | sALS with TDP-43                               | +        | 0        | 0       | 29    |
| M      | 53           | 61           | sALS with TDP-43                               | +        | 0        | 0       | 13    |
| M      | 71           | 73           | sALS with TDP-43                               | 0        | +        | 0       | 23    |
| M      | 61           | 64           | sALS with TDP-43                               | 0        | +        | 0       | 14    |
| M      | 59           | 64           | sALS with TDP-43                               | +        | ++       | +       | 19    |
| M      | 37           | 40           | sALS with TDP-43                               | +        | ++       | +       | 19    |
| M      | 55           | 57           | fALS with TDP-43                               | +        | +++      | 0       | 18    |
| F      | 78           | 82           | fALS with TDP-43                               | ++       | 0        | 0       | 36    |
| F      | 62           | 64           | sALS with TDP-43                               | +        | +        | 0       | 19    |
| M      | N/A          | 54           | Normal control                                 | 0        | 0        | 0       | 12    |
| M      | N/A          | 72           | Normal control                                 | 0        | 0        | 0       | 14    |
| F      | N/A          | 45           | Normal control                                 | 0        | 0        | 0       | 15    |
| F      | N/A          | 78           | Normal control                                 | 0        | 0        | 0       | 8     |

The table of postmortem human samples used in this study. Information about age, sex, clinical diagnosis and the type of TDP-43 pathology is included

NCIs neuronal cytoplasmic inclusions, GCIs glial/microglial cytoplasmic inclusions, DNs extracellular dystrophic neuritis, PMI/h postmortem interval in hours

consequences of TDP-43 pathology with respect to upper motor neuron vulnerability.

## Methods

### Postmortem human brain samples

Postmortem human tissue was collected according to protocols approved by Northwestern University's Institutional Review Board. Clinical records were available for every subject. A neuropathologist with expertise in neurodegenerative disorders examined all samples. Brains were fixed either in 10% neutral buffered formalin for 2 weeks or 4% paraformaldehyde (PFA) at 4 °C for 30 h, and sections were paraffin embedded. Areas of the primary motor cortex (Brodmann area 4) were retrieved, 4- $\mu$ m-thick serial sections were cut, mounted on a charged glass slide (Fisher Scientific, Rockford, IL, USA), and used for immunocytochemical analyses.

In this study, motor cortex isolated from normal control subjects with no neurologic disease as well as sALS patients with cortex involvement and TDP-43 pathology was included. Presence of TDP-43 pathology was confirmed by the antibody that is vastly used to identify TDP-43 pathology in humans, i.e., monoclonal TDP-43 antibody pS409/410-2, 1:5000 dilution, AEC chromogen (Cosmo-Bio USA, Carlsbad, CA, USA) [24]. Motor cortex was evaluated for TDP-43 immunoreactivity in neuronal cytoplasmic inclusions (NCIs), glial cytoplasmic inclusions (GCIs) and extracellular dystrophic neurites (DNs). None of the ALS cases had the p62<sup>+</sup>/TDP43<sup>-</sup> pathology observed in brains of patients with C9orf72 hexanucleotide repeat expansion. In addition, fALS cases had a family history of ALS with unknown mutation but did not include *SOD1* mutation or C9orf72 expansion. Detailed information about the normal controls and TDP-43 pathology cases can be found in Table 1.

To further confirm the presence of TDP-43 pathology in the motor cortex, we performed two lines of investigation: (1) the 1- $\mu$ m semi-thin sections used for electron microscopy (EM) analysis were immunostained with TDP-43 antibody (monoclonal TDP-43 antibody pS409/410-2, 1:500 dilution (Cosmo-Bio USA, Carlsbad, CA, USA), and developed with ABC Kit (ABC Elite kit, Vector Laboratories, Burlingame, CA, USA) to visualize Betz cells, their TDP-43 expression levels and the location of the protein; (2) sensitive fluorescent co-immunostaining was performed using Map2 and TDP-43 antibodies to co-label Betz cells and TDP-43, and to assess even the low levels of TDP-43 in the motor cortex. Since TDP-43 pathology is defined by the presence of pTDP-43, diffusion of TDP-43 to the cytoplasm, and presence of TDP-43<sup>+</sup> inclusions, both the cytoplasm and the nucleus were carefully analyzed for the presence of accumulations and large protein aggregates in the Betz

cells and other cells/neurons in the motor cortex. Betz cells were determined by their location, large pyramidal size and prominent apical dendrite in layer 5 of the motor cortex.

### Mice

All animal experiments were performed in compliance with the standards set by National Institutes of Health and were approved by the Northwestern University Animal Care and Use committee. The following mouse strains were used in this study: WT, prp-TDP-43<sup>A315T</sup> (procured from Jackson Laboratory, stock no. 010700), UCHL1-eGFP (generated by the Ozdinler Lab at Northwestern Targeted Mutagenesis Core Facility, now also available at Jackson Laboratory, stock no. 022476). After weaning the pups at P21, they were supplied with additional gel diet (DietGel 76A, ClearH<sub>2</sub>O, ME, USA) to help alleviate gastrointestinal (GI) complications. Male mice die around P80–P90 due to GI problems, but their condition improves upon DietGel supplement. However, in this study males were exclusively used for breeding purposes. The end-stage is expected between P130 and P150. The disease progression is rather stable and comparable among litters. There were no unexpected deaths prior to end-stage, and even though most mice die at P150, about 10–15% die between P130 and P150. We used female mice at P150 in these studies.

Hemizygous UCHL1-eGFP females were bred to hemizygous prp-TDP-43<sup>A315T</sup>-UeGFP mice. Only females were used in this study, and all mice are on a C57/BL6 background. Progeny were initially screened at birth for eGFP expression, using fluorescent flashlight (BlueStar GFP, NightSea, Lexington, MA, USA). DNA was isolated from tail biopsies by precipitation using isopropanol method. Genotyping was performed by polymerase chain reaction (PCR) to detect the presence of UCHL1-eGFP gene (forward'-CCTACGGCG TGCAGTGCTTCAGC-3' and reverse 5'-CGGCGAGCT GCACGCTGCCGTCCTC-3' primers), PCR cycle [94 °C 2 min, (94 °C 30 s, 62 °C 45 s, 72 °C 45 s) for 30 cycles, 72 °C 10 min], and mutant allele (prp-TDP-43<sup>A315T</sup>) (forward 5'-GGATGAGCTGCGGGAGTTCT-3' and reverse 5'-TGCCCATCATACCCCAACTG-3') and [94 °C 3 min, (94 °C 30 s, 58 °C 30 s, 72 °C 30 s) for 35 cycles, 72 °C 2 min].

### Behavioral analyses

#### Grip strength test

The force exerted by both fore and hind limbs of the mice was measured using grip strength meter (47200 Ugo Basile, Italy). The grip strength meter consists of a grasping bar, which is connected to force sensor and peak amplifier. Mice instinctively grasp the grasping bar and when pulled

backward by its tail, it exerts force on grasping bar. The animal resists the backward pull until force overcomes their grip strength. After the animal loses its grip on the bar, the peak amplifier automatically stores the peak full force achieved by the limb. The maximum force exerted by animal is displayed and force is measured in 'g'.

### Rotarod performance test

This test is based on a rotating rod (Rotarod, Ugo Basile, Italy) that accelerates linearly from 4 to 40 rpm. Rotarod test was used to analyze riding time or endurance and motor coordination of the mice. The length of the time mice stays on the accelerating rotating rod measures their motor coordination. Mice were placed on the horizontal accelerating bar and an average time spent on the rotating rod for three consecutive trials was calculated for maximum 300 s.

### Footprint pattern

Footprint pattern is a visual measure of limb coordination. Walking pattern (gait) analysis can be achieved by this test. The paws of the mice are coated with the ink and mice are allowed to walk on blank white sheet of paper making footprint patterns. These footprints show if there is any defect in the mice limb coordination. The fore and hind paws of WT and prp-TDP-43<sup>A315T</sup> mice at the age of P150 were painted with red and black paints, respectively, prior to walking on white paper in an enclosed area. The walking patterns generated by these mice were used to visualize hind limb paralysis.

Mice ( $n \geq 5$  per each group, genotype and time point) were utilized for all behavioral testing.

### CSMN retrograde labeling surgeries

To visualize CSMN of WT and prp-TDP-43<sup>A315T</sup> mice, 160 nL of 0.5% FluoroGold (FG; Fluorochrome LLC, Denver, CO, USA; in 0.9% saline solution) was injected into the corticospinal tract at P30 as previously described [34, 47]. Surgeries were performed on a stereotaxic platform. Microinjections were performed using pulled-beveled glass micropipettes attached to a nanojector (Drummond Scientific, Broomall, PA, USA). Mice ( $n \geq 3$  per each group and genotype) were killed at P60, P90, P120 and P150.

### Tissue collection and processing

Mice were deeply anesthetized with intraperitoneal injection of Ketamine (90 mg/kg, and Xylazine (10 mg/kg; Fort Dodge Animal Health, Fort Dodge, IA, USA) prior to transcardial perfusion with phosphate-buffered saline (PBS) and 4% paraformaldehyde (PFA) in PBS. Intact cortex and spinal

cord were dissected, post-fixed in 4% PFA overnight and stored long term for later use in PBS with 0.01% sodium azide at 4 °C. The brain was sectioned at 50  $\mu$ m using Leica vibratome (Leica VT1000S, Leica Inc., Nussloch, Germany).

### Immunocytochemistry

Floating sections were incubated in blocking solution (PBS, 0.05% bovine serum albumin, 2% fetal bovine serum, 1% Triton X-100 and 0.1% saponin) for 30 min prior to addition of primary antibodies: chicken anti-GFP (1:1000, Abcam, Cambridge, MA, USA), mouse anti-FLAG (1:500, Millipore Sigma, St. Louis, MO, USA), rabbit anti-CHCHD3 (1:100, Proteintech, Rosemont, IL, USA), rabbit anti-calreticulin (1:250, Abcam, Cambridge, MA, USA), chicken anti-Map2 (1:200, Abcam, Cambridge, MA, USA), and rabbit anti-transportin 1 (1:250, Abcam, Cambridge, MA, USA) at 4 °C overnight. After PBS washes, sections were incubated in appropriate secondary antibodies in blocking solution: Alexa Fluor 488 (1:1000, Thermo Fisher Scientific, Rockford, IL, USA), Alexa Fluor 647 (1:1000, Thermo Fisher Scientific, Rockford, IL, USA) and Cy3-conjugated (1:1000, Molecular Probes, Eugene, OR, USA) for 2 h at room temperature (RT). Antigen retrieval with 0.01 M sodium citrate, pH 9, for 3 h in a water bath at 80 °C was performed prior to blocking for rabbit anti-RanGap1 antibody (1:250; Abcam, Cambridge, MA, USA) as previously described [14]. Sections were counterstained with DAPI (1:5000). All sections were mounted on slides and coverslipped with Fluoromount G (Electron Microscopy Sciences, Hatfield, PA, USA).

### Immunocytochemistry in postmortem human samples

Slides were baked for 60 min at 60 °C, deparaffinized with xylene for 5 min, and rehydrated in ethanol (100, 95, 70, and 50%). For antigen retrieval, slides were immersed in 10 mM sodium citrate and subjected to high heat and pressure for 20 min. After cooling, slides were rinsed with PBS for 10 min and blocked with 0.5% bovine albumin serum, 0.1% Triton X-100, and 2% fetal bovine serum in PBS for 30 min and incubated overnight at 4 °C with a mix of primary antibodies anti-Map2 (1:200, Millipore, Temecula, CA, USA), anti-calreticulin (1:200, Abcam, Cambridge, MA, USA), and anti-CHCHD3 (1:750; Proteintech, Rosemont, IL, USA). After PBS rinses, slides were incubated with donkey anti-chicken Alexa Fluor 488 (1:1000, Thermo Fisher Scientific, Rockford, IL, USA) and donkey anti-rabbit Alexa Fluor 555-conjugated secondary antibodies (1:1000, Thermo Fisher Scientific, Rockford, IL, USA) diluted in the blocking solution for 2 h at RT. Slides were rinsed in PBS and counterstained with DAPI. Autofluorescence was

quenched with True Black (Biotum, Fremont, CA, USA) according to the manufacturer's instructions and coverslipped with Fluoromount G (Electron Microscopy Sciences, Hatfield, PA, USA).

### Immunocytochemistry coupled with electron microscopy (EM)

In a subset of experiments, immunocytochemistry was followed by EM analysis.

**Human:** motor cortex was dissected from PFA-fixed autopsy brain samples, cut into approximately 1-mm cubes, and post-fixed in 2.5% glutaraldehyde for 2 h at RT. The samples were washed three times with PBS for 10 min each and were processed for embedding in the resin.

**Mice:** mice were perfused with EM grade 4% PFA. One hemisphere of the brain was sectioned at 50  $\mu\text{m}$ , coronally on a vibratome (Leica VT1000S, Leica Inc., Nussloch, Germany). The sections were post-fixed in 2% PFA and 0.5% glutaraldehyde for 1 h, they were cryoprotected with glycerol–dimethylsulfoxide (DMSO) mixture followed by freeze–thaw at least four times and treated with 1% sodium borohydrate. They were then treated with 0.3%  $\text{H}_2\text{O}_2$ –10% methanol in TBS (100 mM Tris–HCl and 150 mM NaCl, pH 7.6) and 5% normal goat serum–1% bovine serum albumin in TBS to block non-specific binding of primary antibody. They were incubated overnight with rat anti-Ctip2 antibody (1:500, Thermo Fisher Scientific, Rockford, IL, USA). Biotinylated goat anti-rat IgG (1:500, Vector Laboratories, Burlingame, CA, USA) were used as secondary antibody, and diaminobenzidine (DAB) was applied as the chromogen (ABC Elite kit, Vector Laboratories, Burlingame, CA, USA). Sections were then post-fixed in buffered 2% osmium tetroxide ( $\text{OsO}_4$ ) (Electron Microscopy Sciences, Hatfield, PA, USA), rinsed with distilled water and stained in 1% uranyl acetate (Electron Microscopy Sciences, Hatfield, PA, USA), again rinsed with distilled water, dehydrated in ascending grades of ethanol with transition fluid propylene oxide (Electron Microscopy Sciences, Hatfield, PA, USA) and embedded in resin mixture with Embed 812 (Electron Microscopy Sciences, Hatfield, PA, USA) and cured in a 60 °C oven for 3 days. The sections in which primary motor cortex was present and visible under bright-field illumination on a dissecting scope were selected. Approximately, 5-mm-wide  $\times$  7-mm-long piece of the motor cortex from these sections was dissected under the microscope mounted on resin block and was sectioned on a Leica Ultracut UC6 ultramicrotome (Leica Inc., Nussloch, Germany). 70 nm thin sections were collected on 200-mesh copper–palladium grids. Grids were counterstained with 8% radioactive depleted uranyl acetate and 0.2% lead citrate. Grids were examined on FEI Tecnai Spirit G2 TEM (FEI company, Hillsboro, OR, USA), and digital images were captured on

a FEI Eagle camera. Samples were processed for TEM by the Center for Advanced Microscopy/Nikon Imaging Center (CAM), at Northwestern University Feinberg School of Medicine, Chicago.

### Imaging

Nikon Eclipse TE2000-E (Nikon Inc., Melville, NY, USA), Leica TCS SP5 confocal microscope (Leica Inc., Bensheim, Germany) and Zeiss 880 confocal microscope (Carl Zeiss microscopy, Jena, Germany) were used to acquire low- and high-magnification images, respectively. Z-stacks were processed using ImageJ (National Institutes of Health, Bethesda, MD, USA, <http://imagej.nih.gov/ij>) to generate maximum intensity projections.

### Quantification and data analysis

#### CSMN quantification

CSMN of P30, P60, P90, P120 and P150 WT-UeGFP and prp-TDP-43<sup>A315T</sup>-UeGFP mice ( $n = 3$ ) were counted using maximum projection images acquired from 50- $\mu\text{m}$  sections. An equivalent area of the motor cortex (1.55 mm  $\times$  1.55 mm area corresponding to the 10 $\times$  objective field size) was defined in three serial sections ( $\sim$ 600  $\mu\text{m}$  apart) per mouse. Neurons with pyramidal morphology and a visible apical dendrite were counted in each area, with experimenter blind to age and genotype of mice.

#### Soma area analysis

Motor cortex was imaged in three 50 $\mu\text{m}$  sections per mouse ( $\sim$ 600  $\mu\text{m}$  apart) (WT-UeGFP and prp-TDP-43<sup>A315T</sup>-UeGFP mice,  $n = 3$ ) with a 10 $\times$  objective. Z-stacks were processed with ImageJ software to generate maximum intensity projections. Mean soma area was quantified for each genotype.

#### Nuclear area analysis

Electron microscopy images of Betz cells of normal control and patients, and Ctip2-positive CSMN of WT and prp-TDP-43<sup>A315T</sup> mice were taken on FEI Tecnai Spirit G2 TEM using FEI Eagle camera. Images were calibrated for pixel ratio using ImageJ software. After calibration, the periphery of the nucleus was traced and its area was recorded. Subsequently, a circle was placed as such that entirely covering the nucleus and area of the circle was measured. Percent difference in the area of circle and area of nucleus was calculated and reported as percent deviation from full circle.

## Nuclear membrane integrity

Motor cortex of WT-UeGFP and prp-TDP-43<sup>A315T</sup>-UeGFP mice ( $n=3$ ) was imaged in three 50- $\mu\text{m}$  sections per mouse ( $\sim 600 \mu\text{m}$  apart) using 10 $\times$  objective of field. Z-stacks were processed to generate maximum intensity projection. CSMN expressing RanGap1 were counted using photoshop software (Adobe photoshop, San Jose, CA, USA). RanGap1 expression restricted around nucleus was considered as normal, whereas RanGap1 expression diffused in nucleus and cytoplasm was counted as abnormal.

## Analysis of mitochondria

Motor cortex of WT-UeGFP and prp-TDP-43<sup>A315T</sup>-UeGFP mice, at P30 and P60 ( $n=3$  for each time point and genotype), was imaged in three 50- $\mu\text{m}$  sections per mouse ( $\sim 600 \mu\text{m}$  apart) using 10 $\times$  objective of field. Numbers of CSMN expressing CHCHD3 were counted in both WT-UeGFP and prp-TDP-43<sup>A315T</sup>-UeGFP mice, and expressed as percentage of CSMN expressing CHCHD3. EM images of Betz cells of normal control and patients, and Ctip2-positive CSMN of WT and prp-TDP-43<sup>A315T</sup> mice were taken on FEI Tecnai Spirit G2 TEM using FEI Eagle camera. Mitochondria with apparent morphological defects were count individually and were reported as percentage of defective mitochondria.

## Statistical analysis

Statistical analyses were performed to determine behavioral defects, timing and extent of upper motor neuron degeneration in prp-TDP-43<sup>A315T</sup>-UeGFP mice, the extent of nuclear membrane deformity, and the health of mitochondria. Prism software (GraphPad Software Inc., La Jolla, CA, USA) was used for all statistical analyses. For each quantification, at least  $n=3$  mice were used for each genotype and group. Statistical analyses were based on the average numbers for each mouse, and not based on total individual number of cells or organelle. D'Agostino and Pearson normality tests were performed on all data sets. Either Student's  $t$  test or ANOVA with post hoc Tukey's multiple comparison test was used to determine statistical differences between experimental groups depending on the genotype, experimental conditions and the disease group. Data are shown as mean  $\pm$  SEM of at least three replicates and are representative of three independent experiments unless otherwise stated and statistically significant differences were taken at  $p < 0.05$ , and  $p$  values or adjusted  $p$  values are reported in the text.

## Results

### Betz cells of patients with TDP-43 pathology display unique cellular defects

TDP-43 pathology has been previously observed in different regions of ALS and FTLN patient brains, including motor cortex [44]. Since the presence of TDP-43<sup>+</sup> inclusions is one of the most common pathologies in ALS and other related diseases, we first investigated the presence of p-TDP-43 accumulations in layer 5 of the motor cortex (Brodmann area 4). pTDP-43 accumulations, as detected with pS409/410-2 antibody, were present in neuronal cytoplasmic inclusions (NCIs; Fig. 1a, arrows), glial cytoplasmic inclusions (GCIs) and/or extracellular dystrophic neurites (DNs). Only motor cortices of ALS patients with confirmed TDP-43 pathology are included in this study (Table 1). Since there is well-reported heterogeneity of TDP-43 pathology either by expression of pTDP43, diffusion of pTDP-43 to the cytoplasm, or presence of TDP-43<sup>+</sup> inclusions in the cytoplasm and/or nucleus [7], we have taken two independent lines of investigation to assess whether Betz cells display signs of TDP-43 pathology especially in cases with NCIs. First, we performed pre-embedding immunostaining for TDP-43, embedded the tissue in resin, and sectioned into 1- $\mu\text{m}$  semi-thin sections. Rather than moving forward with EM, we investigated the TDP-43 expression in these sections using a colorimetric detection (Fig. 1b). In patients with NCI type of TDP-43 pathology, among all cells and neurons labeled with TDP-43, the largest neurons in layer 5 of the motor cortex were positive for TDP-43, albeit at different levels and intensities (Fig. 1b). TDP-43 was present mostly in the cytoplasm, suggesting the presence of TDP-43 pathology in Betz cells. When blocks were used for EM analysis, Betz cells were identified based on their size and location (Supplementary Fig. 1). These neurons, different from other cells and neurons located in close vicinity, displayed signs of massive neurodegeneration (Fig. 1c), where the cytoplasm was accumulated with large lipid droplets and autophagolysosomes (Fig. 1c–f). Such defects were not observed in Betz cells of control cases.

Since fluorescence immunocytochemistry is more sensitive than colorimetric detection, we next performed co-immunostaining with Map2 and TDP-43 antibodies using 5- $\mu\text{m}$ -thick sections. Betz cells were the largest pyramidal neurons in layer V of the motor cortex, and they expressed Map2, had diffuse and low levels of TDP-43 expression only in the nucleus (Fig. 2a, h; arrows). Since pS409/410-2 antibody labels mostly p-TDP-43, but also non-phosphorylated TDP-43 at low levels [24], we reasoned that we would be detecting the non-phosphorylated TDP-43 in

## Motor cortex of patients with TDP-43 pathology

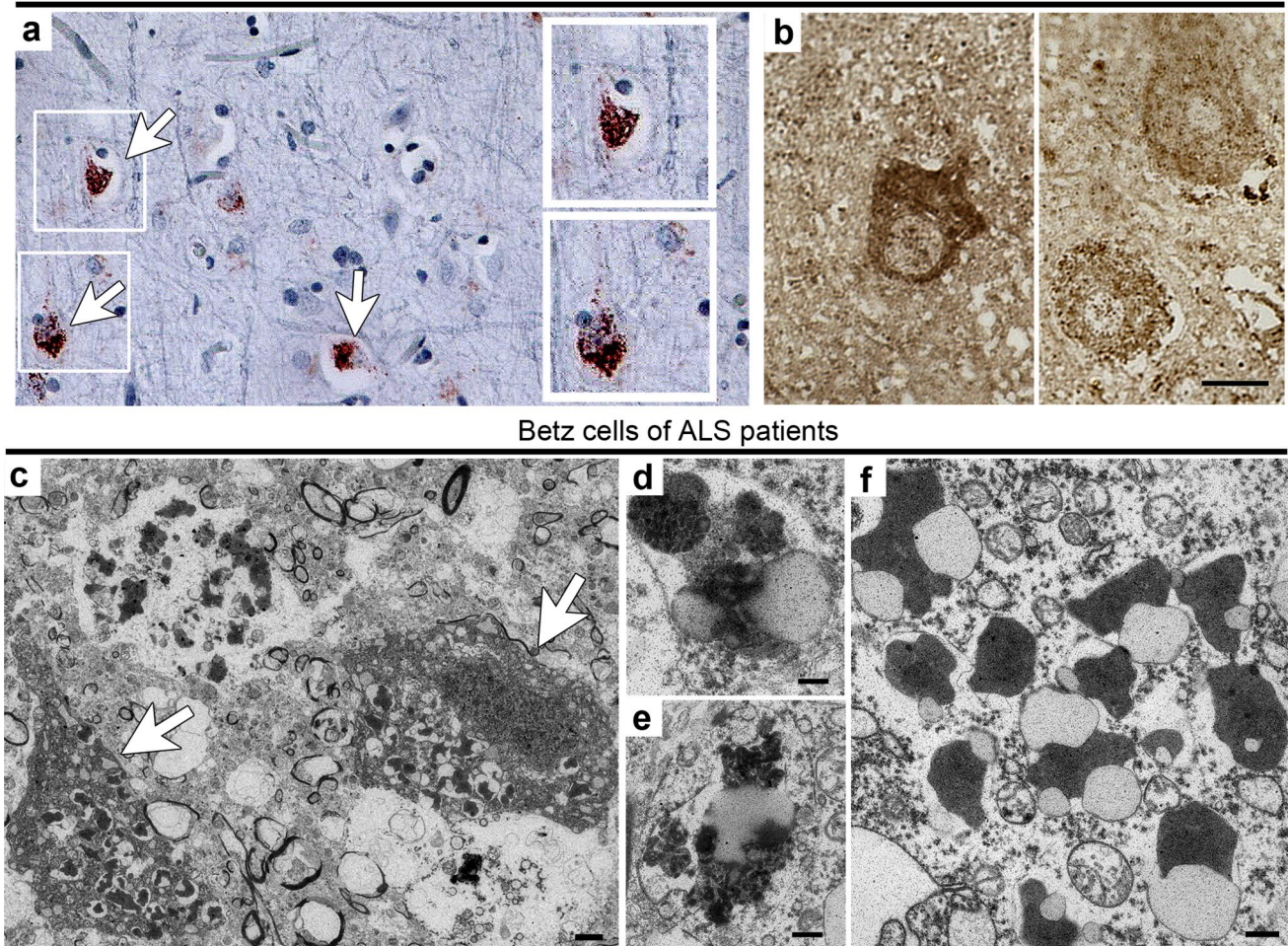


**Fig. 1** Betz cells of patients display TDP-43 pathology and undergo degeneration. **a** Motor cortex of patients shows aggregates of phosphorylated TDP-43, confirming TDP-43 pathology (arrows, enlarged to the side). **b** Pre-embedding immunostaining followed by semithin sectioning shows phosphorylated TDP-43 immunoreactivity in

Betz cells of ALS patients. **c** EM images show degenerating Betz cells (white arrows). **d–f** Betz cells are filled with membrane bound vesicles consisting of electron-dense material, which appears to be autophagolysosomes. Scale bars: **b–d** = 20  $\mu$ m; **c–f** = 500 nm

the nucleus of Betz cells of control cases (Fig. 2b, c, h). However, Betz cells of patients, especially with NCI type of TDP-43 inclusions, had very strong accumulations both in the nucleus and the cytoplasm (Fig. 2e, f, g, i, j). The nuclear and cytoplasmic inclusions were amorphous coarse filamentous structures, suggesting the presence of protein accumulations (Fig. 2e–g, arrows). Interestingly, as the Betz cells displayed signs of degeneration with reduced Map2 expression, apical dendrite disintegration, and shrinkage of soma, the presence of TDP-43 in the cytoplasm was increased (Fig. 2i, j). However, nearby cells and neurons did not have similar expression patterns (Fig. 2f, g). Non-Betz cells or other non-neuronal cells had diffuse and low-level nuclear TDP-43 expression as healthy cells and neurons do [4]. These results suggest

that TDP-43 pathology is observed in varying degrees and extent, especially in cases of patients with NCIs.

Since TDP-43 pathology has been attributed to nuclear membrane defects and problems with nucleocytoplasmic transport system [13, 35], we first investigated the nuclear membrane of Betz cells in both control and TDP-43 cases. Nuclear membranes of Betz cells in normal controls were almost perfect circle and no defects were observed (Fig. 3a). However, the nucleus of Betz cells with TDP-43 pathology appeared smaller, wrinkled and amorphous (Fig. 3b). In contrast, other non-Betz cells that are located next to Betz cells in the motor cortex of patients with TDP-43 were similar to control cases (Fig. 3c). A closer look revealed the presence of large blebs along the nuclear membrane towards the cytoplasm of only the Betz cells of patients with TDP-43

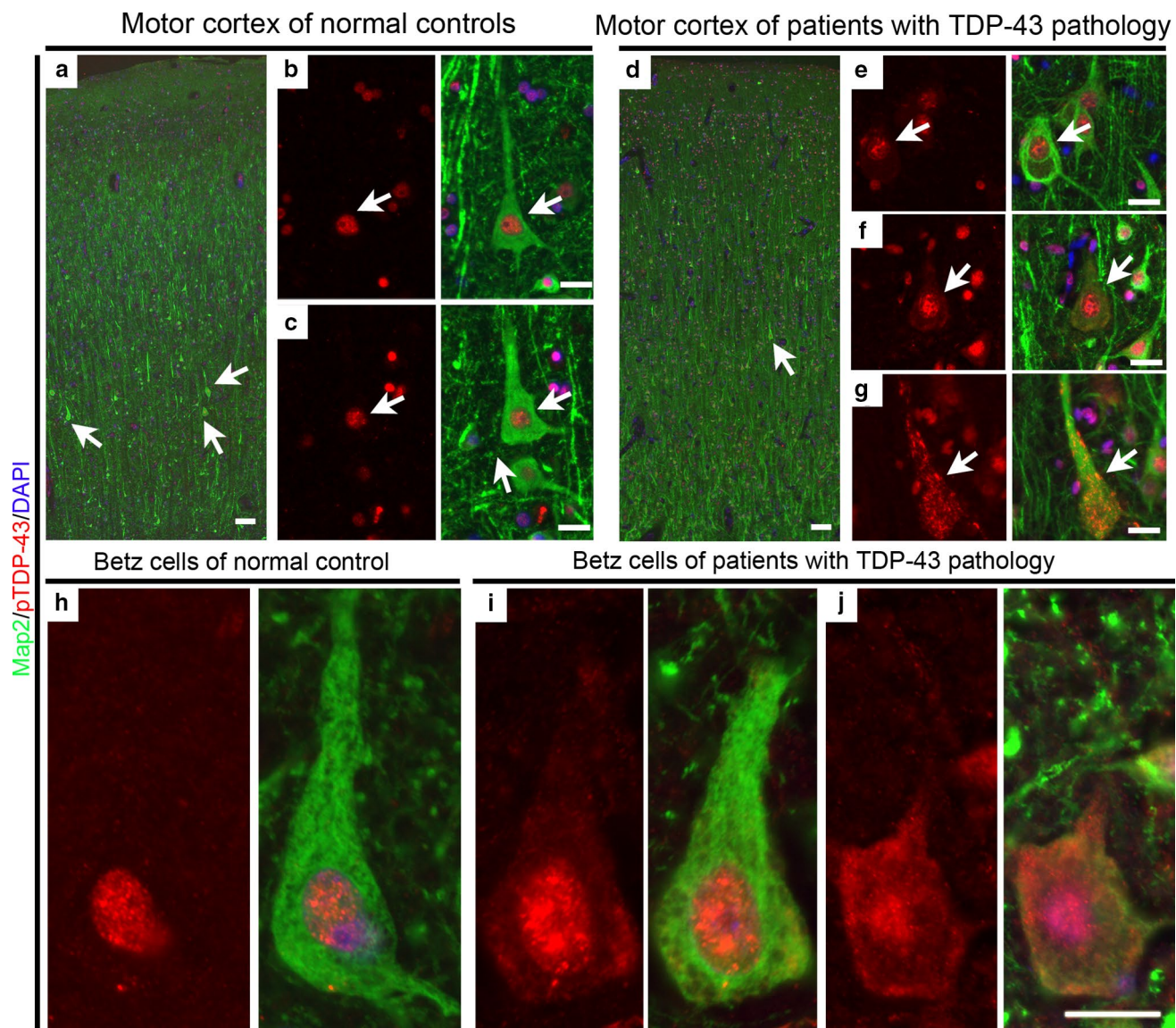


**Fig. 2** Betz cells display mislocalized TDP-43 in patients with TDP-43 pathology. **a** Map2<sup>+</sup> large pyramidal Betz cells are located in layer 5 (arrows) of motor cortex in normal control cases. **b, c** Map2 (green) and pTDP-43 (red) co-labeling shows low levels of TDP-43 expression in the nucleus of Betz cells in normal controls (arrows). **d** A representative image showing the motor column of patients with TDP-43 pathology. Betz cells are marked with Map2 (green, arrow).

**e–g** Examples of diseased Betz cells with increased nuclear (**e, f**) or cytoplasmic (**f, g**) TDP-43<sup>+</sup> accumulation. **h** Enlarged view of normal control Betz cell with low levels of TDP-43 in their nucleus. Enlarged view of diseased Betz cells with increased levels of TDP-43 expression in the nucleus (**i**) and accumulation in the cytoplasm (**j**). Scale bar: **a, d** = 100  $\mu$ m; **b, c, e–j** = 20  $\mu$ m

pathology (Fig. 3d–f, white arrows). There were dark accumulations especially on the nuclear face of the space between the double lipophilic membrane (Fig. 3f, arrow). Nuclear area was significantly reduced in Betz cells of ALS patients with TDP-43 pathology (control  $89.3 \pm 3.4 \mu\text{m}^2$ ,  $n=3$  normal control; ALS  $63.2 \pm 1.9 \mu\text{m}^2$ ,  $n=4$  patients; ANOVA followed by Tukey's multiple comparison test, adjusted  $p$  value = 0.0019; Fig. 3g), but nuclei of non-Betz cells were comparable to control cases (non-Betz cells  $72.8 \pm 4.6 \mu\text{m}^2$ ,  $n=4$  patients; Fig. 3h). The nuclear

shape of diseased Betz cells significantly deviated from full circle (control  $8.6 \pm 0.9\%$  deviation,  $n=3$  control subjects; ALS  $37.7 \pm 1.9\%$  deviation,  $n=4$  patients; ANOVA followed by Tukey's multiple comparison test, adjusted  $p$  value < 0.0001). However, nuclear membranes of Betz cells from normal control subjects and that of non-Betz cells from ALS patients with TDP-43 pathology ( $7.6 \pm 2.4\%$  deviation,  $n=4$  patients) were comparable (adjusted  $p$  value = 0.9467). These EM analyses corroborated with findings reporting nuclear membrane defects with TDP-43 pathology [7, 36,



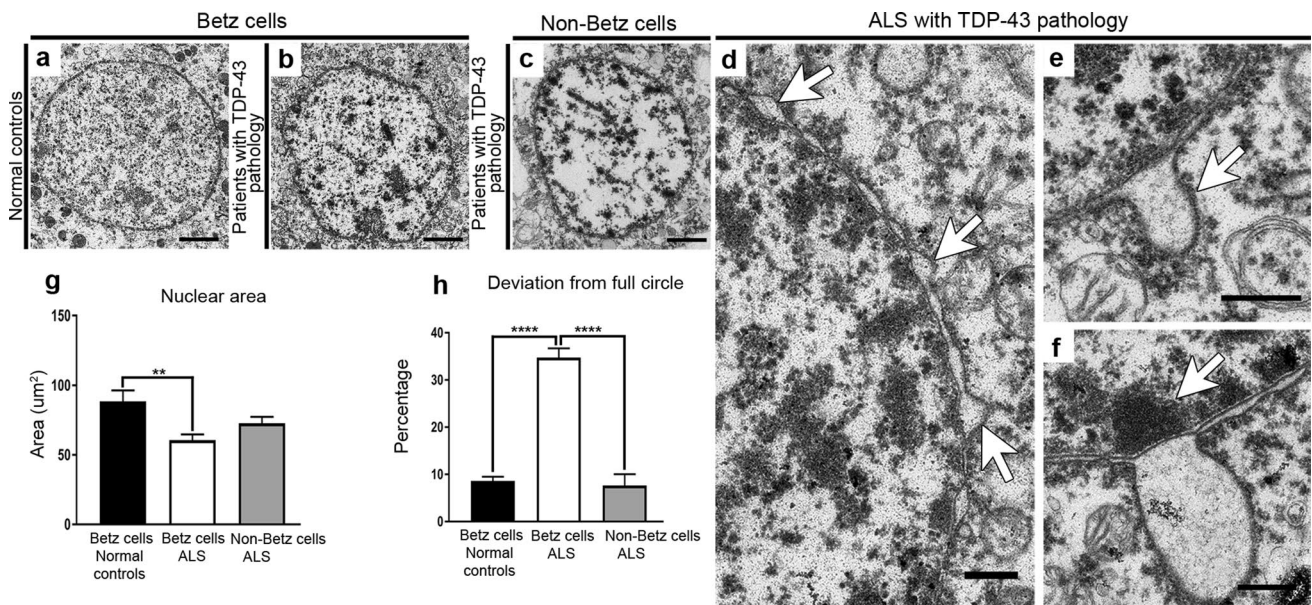


**Fig. 3** Betz cells display abnormal nuclear morphology due to TDP-43 pathology. **a** Nucleus of Betz cells from normal control was spherical without any defects, **b** unlike nucleus of Betz cells from patients which showed crinkled and invaginated nuclear membrane. **c** However, nucleus of non-Betz cells from patients looks healthy without any defects. **d–f** Magnified views of nuclear membrane of patient Betz cells displaying large blebbing **g** Graph represents the average nuclear area SEM in Betz cells of normal controls (black column), in

Betz cells of ALS (white column), and non-Betz cells of ALS (gray column). **h** Graph represents the average percentage of the deviation from full circle SEM in Betz cells of normal controls (black column), in Betz cells of ALS (white column), and non-Betz cells of ALS (gray column). Scale bars: **a–k** = 500 nm. Data shown represent three replicates and at least three independent experiments. \*\*  $p < 0.01$ , \*\*\*\*  $p < 0.0001$

45], and gave us the confidence to further investigate cellular defects that occur in upper motor neurons.

### Generation and characterization of CSMN reporter line with TDP-43 pathology

In an effort to reveal the mechanisms associated with TDP-43 pathology, numerous mouse models have been generated with a varying degree of pathology [2, 11, 30, 32, 61, 64, 66, 73–75]. prp-TDP-43<sup>A315T</sup> mice were developed based on the mutation detected in ALS patients with TDP-43 pathology. They mimic many aspects of motor neuron disease in patients, display a robust and progressive motor function defects, and suggest degeneration of upper motor neurons [72]. Therefore, we decided to utilize this mouse model in our efforts to assess the underlying cellular defects that cause CSMN vulnerability.

The prp-TDP-43<sup>A315T</sup> mice displayed clinching and clasping behavior (Fig. 4a), they dragged their feet during end-stage, and displayed gait and walking problems (Fig. 4b), similar to previously reported ALS mouse models [18, 25, 64, 74, 75]. To further assess the timing and the extent of their motor function defects, changes in rotarod (Fig. 4c) and grip strength (Fig. 4d) were evaluated at P21, P30, P60, P90, P120 and P150. There were no motor function defects by

rotarod at P21 (WT  $265 \pm 10$  s,  $n = 7$  mice; prp-TDP-43<sup>A315T</sup>  $244 \pm 6$  s,  $n = 7$  mice; Fig. 4c). However, there was a steady decline in the time mice spent on rotarod, starting at P30 (WT  $259 \pm 5$  s,  $n = 7$  mice; prp-TDP-43<sup>A315T</sup>  $199 \pm 5$  s,  $n = 7$  mice, ANOVA followed by Tukey's multiple comparison test adjusted  $p$  value  $< 0.0001$ ; Fig. 4c) and progressing by P60 (WT  $275 \pm 4$  s,  $n = 8$  mice; prp-TDP-43<sup>A315T</sup>  $204 \pm 6$  s,  $n = 7$  mice; ANOVA followed by Tukey's multiple comparison test, adjusted  $p$  value  $< 0.0001$ ; Fig. 4c), P90 (WT  $238 \pm 8$  s,  $n = 8$  mice; prp-TDP-43<sup>A315T</sup>  $153 \pm 5$  s,  $n = 6$  mice; ANOVA followed by Tukey's multiple comparison test, adjusted  $p$  value  $< 0.0001$ ; Fig. 4c), P120 (WT  $279 \pm 9$  s,  $n = 11$  mice; prp-TDP-43<sup>A315T</sup>  $124 \pm 9$  s,  $n = 9$  mice; ANOVA followed by Tukey's multiple comparison test, adjusted  $p$  value  $< 0.0001$ ; Fig. 4c) and P150 (WT  $232 \pm 18$  s,  $n = 5$  mice; prp-TDP-43<sup>A315T</sup>  $10 \pm 2$  s,  $n = 8$  mice; ANOVA followed by Tukey's multiple comparison test, adjusted  $p$  value  $< 0.0001$ ; Fig. 4c). Grip strength analysis also revealed differences between healthy and diseased mice, starting as early as P60. WT and prp-TDP-43<sup>A315T</sup> mice were comparable at P21 (WT  $23.16 \pm 0.86$  g,  $n = 7$  mice; prp-TDP-43<sup>A315T</sup>  $21.79 \pm 0.47$  g,  $n = 7$  mice; Fig. 4d) and P30 (WT  $22.87 \pm 0.58$  g,  $n = 7$  mice; prp-TDP-43<sup>A315T</sup>  $21.46 \pm 0.59$  g,  $n = 7$  mice; Fig. 4d). However, the difference between WT and prp-TDP-43<sup>A315T</sup> mice became more evident by P60 (WT  $26.88 \pm 1.24$  g,  $n = 8$

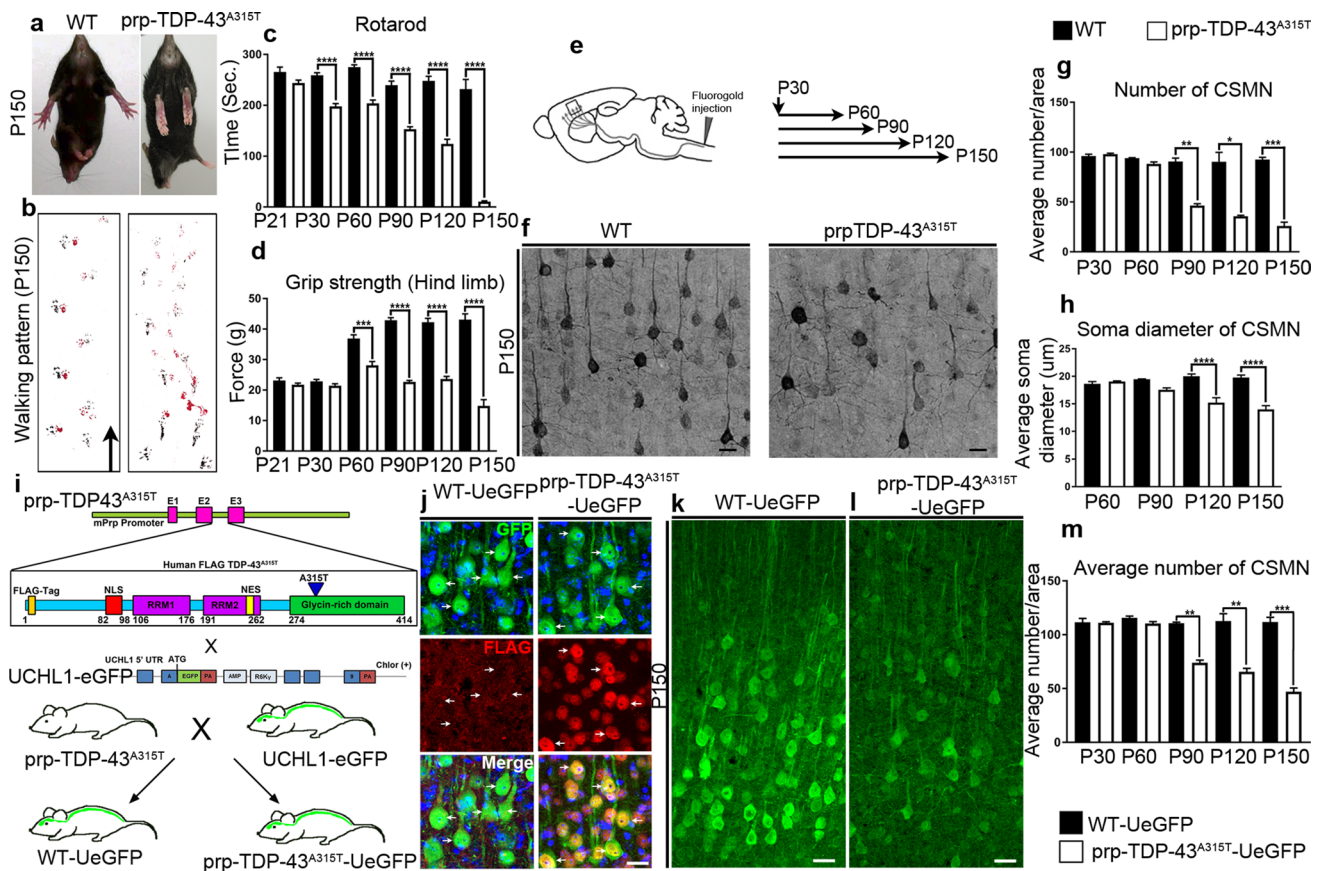


**Fig. 4** Mouse model of ALS expressing mutated human TDP-43<sup>A315T</sup> displays motor function defects and progressive degeneration of CSMN. **a** Representative screen captures of posture in WT and prp-TDP-43<sup>A315T</sup> mice tail-hanging at P150 showing hind limb clasp. **b** Directional walking patterns of WT and prp-TDP-43<sup>A315T</sup> mice showing dragging of hind limbs at P150. **c** Quantitative analysis of Rotarod test in WT and prp-TDP-43<sup>A315T</sup> at P21, P30, P60, P90, P120, and P150. **d** Quantitative analysis of hind limb grip test in WT and prp-TDP-43<sup>A315T</sup> at P21, P30, P60, P90, P120, and P150. **e** Schematic diagram of experimental design for CSMN retrograde labeling by FluoroGold. **f** Representative images of matching coronal motor cortices of WT and prp-TDP-43<sup>A315T</sup> mice at P150 showing labeled CSMN with FluoroGold. Quantitative analysis of average numbers of CSMN (**g**) and average CSMN soma diameter (**h**) shows a decrease

of both parameters in prp-TDP-43<sup>A315T</sup> CSMN starting at P90. **i** Drawing of prp-TDP-43<sup>A315T</sup> gene showing location of FLAG-tag sequence and insertion of A315T mutation. Breeding strategy to generate prp-TDP-43<sup>A315T</sup>-UeGFP mice. **j** Representative images showing immunocytochemistry of eGFP with or without co-localization of FLAG in CSMN of WT and prp-TDP-43<sup>A315T</sup> mice to confirm FLAG protein sequence and expression of prp-TDP-43<sup>A315T</sup> gene in prp-TDP-43<sup>A315T</sup>-UeGFP mice. **k, l** Representative images of matching coronal motor cortices of WT-UeGFP and prp-TDP-43<sup>A315T</sup>-UeGFP mice used for (**m**) quantitative analysis of average numbers of CSMN in prp-TDP-43<sup>A315T</sup>-UeGFP. Scale bars: **f**=50 μm; **j**=10 μm; **k, l**=50 μm. Bar graphs represent mean ± SEM of at least three replicates. \*\*\*\*  $p < 0.0001$

mice; prp-TDP-43<sup>A315T</sup> 28.11 ± 1.26 g,  $n = 7$  mice; ANOVA followed by Tukey's multiple comparison test, adjusted  $p$  value < 0.0001; Fig. 4d), and progressively worsened by P90 (WT 42.91 ± 0.80 g,  $n = 8$  mice; prp-TDP-43<sup>A315T</sup> 22.7 ± 0.43 g,  $n = 7$  mice; ANOVA followed by Tukey's multiple comparison test, adjusted  $p$  value < 0.0001; Fig. 4d), P120 (WT 42.24 ± 1.26 g,  $n = 11$  mice; prp-TDP-43<sup>A315T</sup>: 23.64 ± 0.84 g,  $n = 9$  mice; ANOVA followed by Tukey's multiple comparison test, adjusted  $p$  value < 0.0001; Fig. 4d) and P150 (WT 43.1 ± 1.88 g,  $n = 5$  mice; prp-TDP-43<sup>A315T</sup> 14.83 ± 2.05 g,  $n = 8$  mice; ANOVA followed by Tukey's multiple comparison test, adjusted  $p$  value < 0.0001; Fig. 4d).

We next investigated the timing and the extent of CSMN degeneration in prp-TDP-43<sup>A315T</sup> mice by Fluoro-Gold (FG) retrograde labeling at P30, (Fig. 4e) as previously described [33, 34]. CSMN numbers were quantitatively assessed at P60, P90, P120 and P150. To investigate CSMN at P30, mice were injected with FG at P21. CSMN were visualized in layer 5 of the motor cortex in both WT and prp-TDP-43<sup>A315T</sup> mice (Fig. 4f). CSMN numbers were comparable between WT and prp-TDP-43<sup>A315T</sup> mice at P30 (WT 96 ± 2,  $n = 3$  mice; prp-TDP-43<sup>A315T</sup> 98 ± 1,  $n = 3$  mice; Fig. 4g) and P60 (WT 94 ± 1,  $n = 3$  mice; prp-TDP-43<sup>A315T</sup> 88 ± 2,  $n = 3$  mice; Fig. 4g). However, there was a progressive decline in CSMN numbers by P90 (WT 90 ± 3,

$n = 3$  mice; prp-TDP-43<sup>A315T</sup>  $46 \pm 2$ ,  $n = 3$  mice; ANOVA followed by Tukey's multiple comparison test, adjusted  $p$  value  $< 0.0001$ ; Fig. 4g), and phenotype became more severe by P120 (WT  $90 \pm 9$ ,  $n = 3$  mice; prp-TDP-43<sup>A315T</sup>  $36 \pm 1$ ,  $n = 3$  mice; ANOVA followed by Tukey's multiple comparison test, adjusted  $p$  value  $< 0.0001$ ; Fig. 4g) and P150 (WT  $93 \pm 2$ ,  $n = 3$  mice; prp-TDP-43<sup>A315T</sup>  $26 \pm 4$ ,  $n = 3$  mice; ANOVA followed by Tukey's multiple comparison test, adjusted  $p$  value  $< 0.0001$ ; Fig. 4g). CSMN soma diameter analysis also revealed an ongoing cellular degeneration (P60: WT  $18.6 \pm 0.4$   $\mu\text{m}$ ,  $n = 3$  mice; prp-TDP-43<sup>A315T</sup>  $19 \pm 0.1$   $\mu\text{m}$ ,  $n = 3$  mice; P90: WT  $19.4 \pm 0.07$   $\mu\text{m}$ ,  $n = 3$  mice; prp-TDP-43<sup>A315T</sup>  $17.5 \pm 0.3$   $\mu\text{m}$ ,  $n = 3$  mice; P120: WT  $20 \pm 0.4$   $\mu\text{m}$ ,  $n = 3$  mice and prp-TDP-43<sup>A315T</sup>  $15.2 \pm 0.8$   $\mu\text{m}$ ,  $n = 3$  mice; ANOVA followed by Tukey's multiple comparison test, adjusted  $p$  value  $< 0.0001$ ) and P150 (WT  $19.7 \pm 0.4$   $\mu\text{m}$ ,  $n = 3$  mice, and prp-TDP-43<sup>A315T</sup>  $13.9 \pm 0.6$   $\mu\text{m}$ ,  $n = 3$  mice, ANOVA followed by Tukey's multiple comparison test, adjusted  $p$  value  $< 0.0001$ ; Fig. 4h). Statistical analyses are performed based on the number of mice. These results suggested that TDP-43 pathology does not induce a developmental defect on CSMN health in the prp-TDP-43<sup>A315T</sup> mice, but that CSMN undergo progressive cellular degeneration.

In an effort to bring cellular clarity and precise cellular assessment to CSMN with TDP-43 pathology, we generated prp-TDP-43<sup>A315T</sup>-UeGFP mice (Fig. 4i), by crossing prp-TDP-43<sup>A315T</sup> with UCHL1-eGFP mice, a well-characterized reporter line of CSMN [76]. This reporter line was previously used to reveal details of CSMN in hSOD1<sup>G93A</sup> [76] and Alsin<sup>KO</sup> mice [21].

TDP-43 expression within CSMN of prp-TDP-43<sup>A315T</sup>-UeGFP mice was consistent with previous reports [72] (Fig. 4j). eGFP+CSMN were easy to visualize in the motor cortex and suggested a reduction of CSMN numbers in the prp-TDP-43<sup>A315T</sup> mice (Fig. 4k–l). Quantitative assessment showed no change in average CSMN numbers at P30 (WT-UeGFP  $111 \pm 3$  CSMN,  $n = 3$  mice; prp-TDP-43<sup>A315T</sup>-UeGFP  $111 \pm 1$  CSMN,  $n = 3$  mice, Fig. 3m) and P60 (WT-UeGFP  $115 \pm 1$  CSMN,  $n = 3$  mice; prp-TDP-43<sup>A315T</sup>-UeGFP  $110 \pm 1$  CSMN,  $n = 3$  mice, Fig. 4m). The timing and the extent of CSMN degeneration in prp-TDP-43<sup>A315T</sup>-UeGFP mice were comparable to that of prp-TDP-43<sup>A315T</sup> mice (Fig. 4g), and CSMN loss became significant by P90 (WT-UeGFP  $110 \pm 1$  CSMN,  $n = 3$  mice; prp-TDP-43<sup>A315T</sup>-UeGFP  $74 \pm 2$  CSMN,  $n = 3$  mice; ANOVA followed by Tukey's multiple comparison test, adjusted  $p$  value  $< 0.0001$ , Fig. 4m), P120 (WT-UeGFP  $112 \pm 6$  CSMN,  $n = 3$  mice; prp-TDP-43<sup>A315T</sup>-UeGFP  $65 \pm 3$  CSMN,  $n = 3$  mice; ANOVA followed by Tukey's multiple comparison test, adjusted  $p$  value  $< 0.0001$ , Fig. 4m) and P150 (WT-UeGFP  $118 \pm 4$  CSMN,  $n = 3$  mice; prp-TDP-43<sup>A315T</sup>-UeGFP  $47 \pm 3$  CSMN,  $n = 3$  mice; ANOVA followed by

Tukey's multiple comparison test, adjusted  $p$  value  $< 0.0001$ , Fig. 4m).

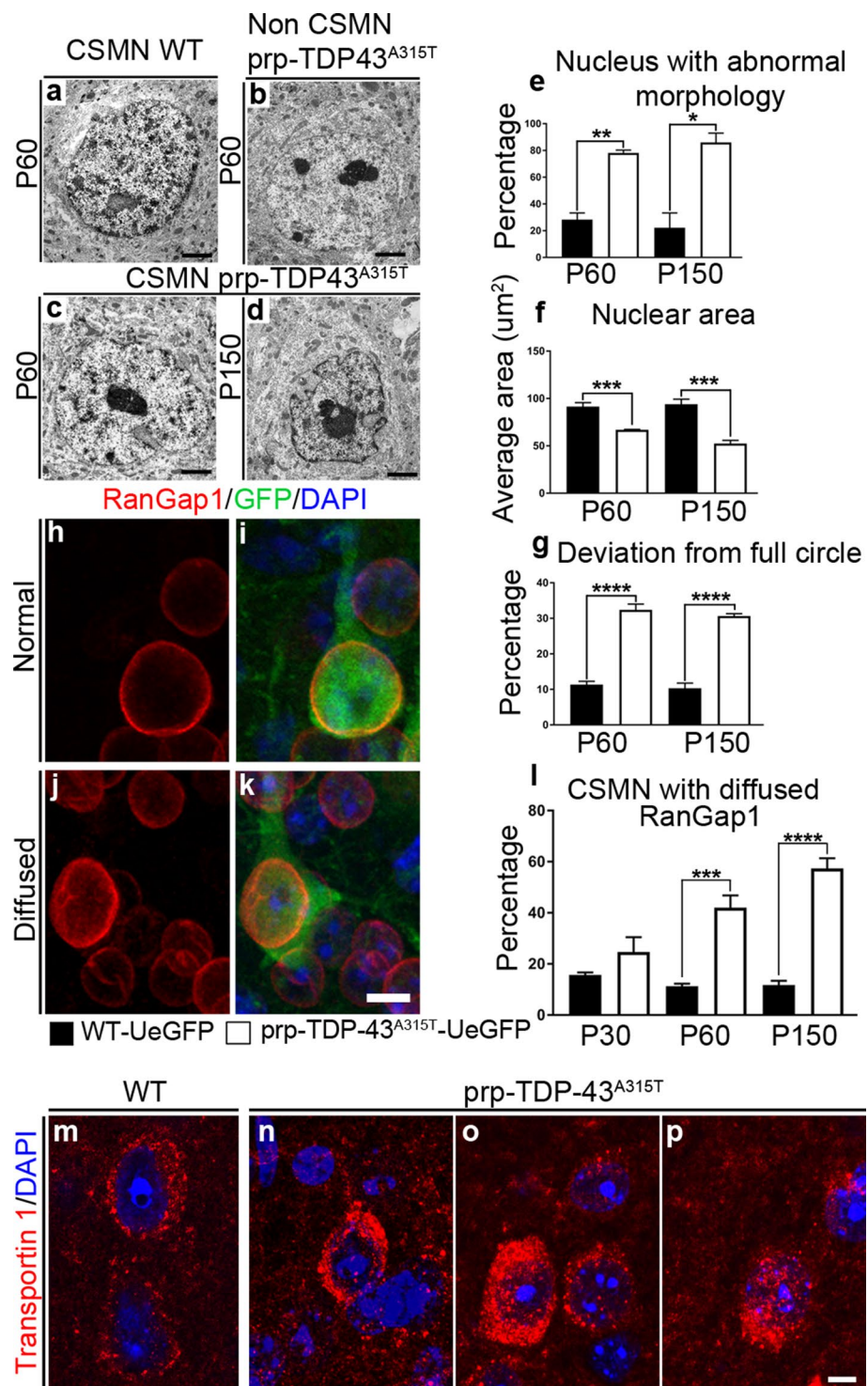
## CSMN of prp-TDP-43<sup>A315T</sup> mice share common cellular pathologies with diseased Betz cells

### Nuclear membrane defects

We next investigated whether CSMN of prp-TDP-43<sup>A315T</sup> mice displayed similar cellular defects observed in the Betz cells of patients with TDP-43 pathology, using immunocoupled EM analysis. Healthy CSMN in WT mice had smooth and round nuclear membranes with normal morphology (Fig. 5a), similar to non-CSMN in the prp-TDP-43<sup>A315T</sup> mice (Fig. 5b). Conversely, the percentage of CSMN with numerous kinks and groves in their nuclear membranes in prp-TDP-43<sup>A315T</sup> mice was significantly higher at P60 (P60: WT  $28.2 \pm 5\%$ ,  $n = 3$  mice; prp-TDP-43<sup>A315T</sup>  $78 \pm 2\%$ ,  $n = 3$  mice; ANOVA followed by Tukey's multiple comparison test, adjusted  $p$  value = 0.005) and continued to increase at P150 (P150: WT  $22 \pm 11\%$ ,  $n = 3$  mice; prp-TDP-43<sup>A315T</sup>  $85.9 \pm 7\%$ ,  $n = 3$  mice; ANOVA followed by Tukey's multiple comparison test, adjusted  $p$  value = 0.0010; Fig. 5c–e). These findings were similar to Betz cells of ALS patients with TDP-43 pathology (Fig. 3b). The nuclear area of CSMN was also reduced already at P60 (P60: WT  $88.6 \pm 0.9$   $\mu\text{m}^2$ ,  $n = 3$  mice; prp-TDP-43<sup>A315T</sup>  $67.6 \pm 1.6$   $\mu\text{m}^2$ ,  $n = 3$  mice; ANOVA followed by Tukey's multiple comparison test, adjusted  $p$  value = 0.0083) and progressively declined by P150 (P150: WT  $89.6 \pm 1.4$   $\mu\text{m}^2$ ,  $n = 3$  mice; prp-TDP-43<sup>A315T</sup>  $69.3 \pm 0.6$   $\mu\text{m}^2$ ,  $n = 3$  mice; ANOVA followed by Tukey's multiple comparison test, adjusted  $p$  value = 0.0003; Fig. 5f). There was a striking percent deviation from full circle at both P60 (WT  $11.4 \pm 0.9\%$ ,  $n = 3$  mice; prp-TDP-43<sup>A315T</sup>  $32.3 \pm 1.6\%$ ,  $n = 3$  mice; ANOVA followed by Tukey's multiple comparison test, adjusted  $p$  value  $< 0.0001$ ; Fig. 4g) and P150 (WT  $10.3 \pm 1.4\%$ ,  $n = 3$  mice; prp-TDP-43<sup>A315T</sup>  $30.6 \pm 0.6\%$ ,  $n = 3$  mice; ANOVA followed by Tukey's multiple comparison test, adjusted  $p$  value  $< 0.0001$ ; Fig. 5g). However, percent deviation from full circle was comparable in non-CSMN both at P60 (WT  $5.11 \pm 0.8\%$ ,  $n = 3$  mice; prp-TDP-43<sup>A315T</sup>  $4.6 \pm 0.7\%$ ,  $n = 3$  mice) and P150 (WT  $5 \pm 0.7\%$ ,  $n = 3$  mice; prp-TDP-43<sup>A315T</sup>  $7.4 \pm 0.2\%$ ,  $n = 3$  mice). These amorphous shapes of CSMN nuclear membrane were almost identical to the defects observed in Betz cells of patients (Fig. 3a–f), suggesting a conserved problem with nuclear/cytoplasmic import and export in upper motor neurons.

In an effort to investigate this possibility, and to reveal the timing and extent of nuclear membrane defects, we studied the distribution of RanGap1 protein at P30, P60 and P150. RanGap1 is normally present around the nuclear membrane (Fig. 5h–i) but is diffused into the

**Fig. 5** TDP-43<sup>A315T</sup> mutation leads to nuclear defects in CSMN of prp-TDP-43<sup>A315T</sup> and prp-TDP-43<sup>A315T</sup>-UeGFP mice. Representative EM images of nuclei of WT CSMN stained with Ctip2 (a) and non-CSMN in TDP-43<sup>A315T</sup> mice Ctip2 negative (b) reveal comparable and healthy nuclear structures. c, d Representative EM images of nuclei of TDP-43<sup>A315T</sup> CSMN stained with Ctip2 at P60 and P150 displaying progressive morphological defects. Quantitative analysis of average nuclei with abnormal morphology (e), average nuclear area (f), and average percentage of deviation from full circle (g) in WT and prp-TDP-43<sup>A315T</sup> CSMN. h–k Representative images showing RanGap1 and eGFP immunocytochemistry where RanGap1 expression is restricted to periphery of nucleus in WT-UeGFP CSMN (h, i), in contrast RanGap1 expression is diffused and filled the nucleus in prp-TDP-43<sup>A315T</sup>-UeGFP CSMN (j, k). l Quantitative analysis of CSMN with diffused RanGap1 expression in WT-UeGFP and prp-TDP-43<sup>A315T</sup>-UeGFP mice. m Representative images showing Transportin 1 is localized around nucleus in WT CSMN, n–p in contrast Transportin 1 is aggregated into the cytoplasm of CSMN of prp-TDP-43<sup>A315T</sup> mice. Scale bars: a–d = 2  $\mu$ m; h–p = 5  $\mu$ m. Bar graphs represent mean  $\pm$  SEM of at least three replicates. \*\*  $p < 0.01$ , \*\*\*  $p < 0.001$ , \*\*\*\*  $p < 0.0001$



nucleus and at times to the cytoplasm [5, 54] (Fig. 5j–k). The percentage of RanGap1 that diffuses into the nucleus and cytoplasm in CSMN was increasingly present at P60 (UeGFP-prp-TDP-43<sup>A315T</sup> 42  $\pm$  4.7%,  $n = 3$  mice; ANOVA followed by Tukey's multiple comparison test, adjusted  $p$  value < 0.0007; Fig. 5l) and P150 (UeGFP-prp-TDP-43<sup>A315T</sup> 57.3  $\pm$  3.9%,  $n = 3$  mice; ANOVA followed by Tukey's multiple comparison test, adjusted  $p$  value < 0.0001; Fig. 5l). In addition, transportin1 was expressed around nucleus in WT CSMN (Fig. 5m), but was mostly accumulated in the cytoplasm of diseased CSMN in prp-TDP-43<sup>A315T</sup> mice (Fig. 5n–p), further implicating nuclear transportation defects. These results strongly suggest

UeGFP-prp-TDP-43<sup>A315T</sup> 57.3  $\pm$  3.9%,  $n = 3$  mice; ANOVA followed by Tukey's multiple comparison test, adjusted  $p$  value < 0.0001; Fig. 5l). In addition, transportin1 was expressed around nucleus in WT CSMN (Fig. 5m), but was mostly accumulated in the cytoplasm of diseased CSMN in prp-TDP-43<sup>A315T</sup> mice (Fig. 5n–p), further implicating nuclear transportation defects. These results strongly suggest

that nucleo-cytoplasmic transport defects occur early, and progressively contribute to neuronal vulnerability.

### Mitochondrial defects

Problems with mitochondrial health were previously reported with respect to TDP-43 pathology [41, 53]. Expression of CHCHD3, a protein that is present in the inner mitochondrial membrane [15], was used to investigate mitochondrial integrity. WT CSMN expressed high levels of CHCHD3, similar to other cells and neurons in the motor cortex (Fig. 6a, arrows and arrowheads, respectively). However, CHCHD3 expression became below detectable levels

in the CSMN of prp-TDP-43<sup>A315T</sup>-UeGFP mice (Fig. 6b–d, arrows), whereas other neighboring cells and neurons were not affected (Fig. 6b–d, arrowheads), suggesting potential mitochondrial defects in CSMN. We utilized CHCHD3 expression for quantitative assessment of CSMN with mitochondrial defects (eGFP<sup>+</sup>/CHCHD3<sup>-</sup> CSMN), which became significant by P60 [P30: WT 18 ± 4%, *n* = 3 mice; prp-TDP-43<sup>A315T</sup> 24 ± 3%, *n* = 3 mice; (Fig. 6n); P60: WT 17 ± 1%, *n* = 3 mice; prp-TDP-43<sup>A315T</sup> 43 ± 1%, *n* = 3 mice; ANOVA followed by Tukey's multiple comparison test, adjusted *p* value = 0.005; Fig. 6n].

EM studies revealed striking mitochondrial damage. Mitochondria of WT CSMN had an intact outer membrane

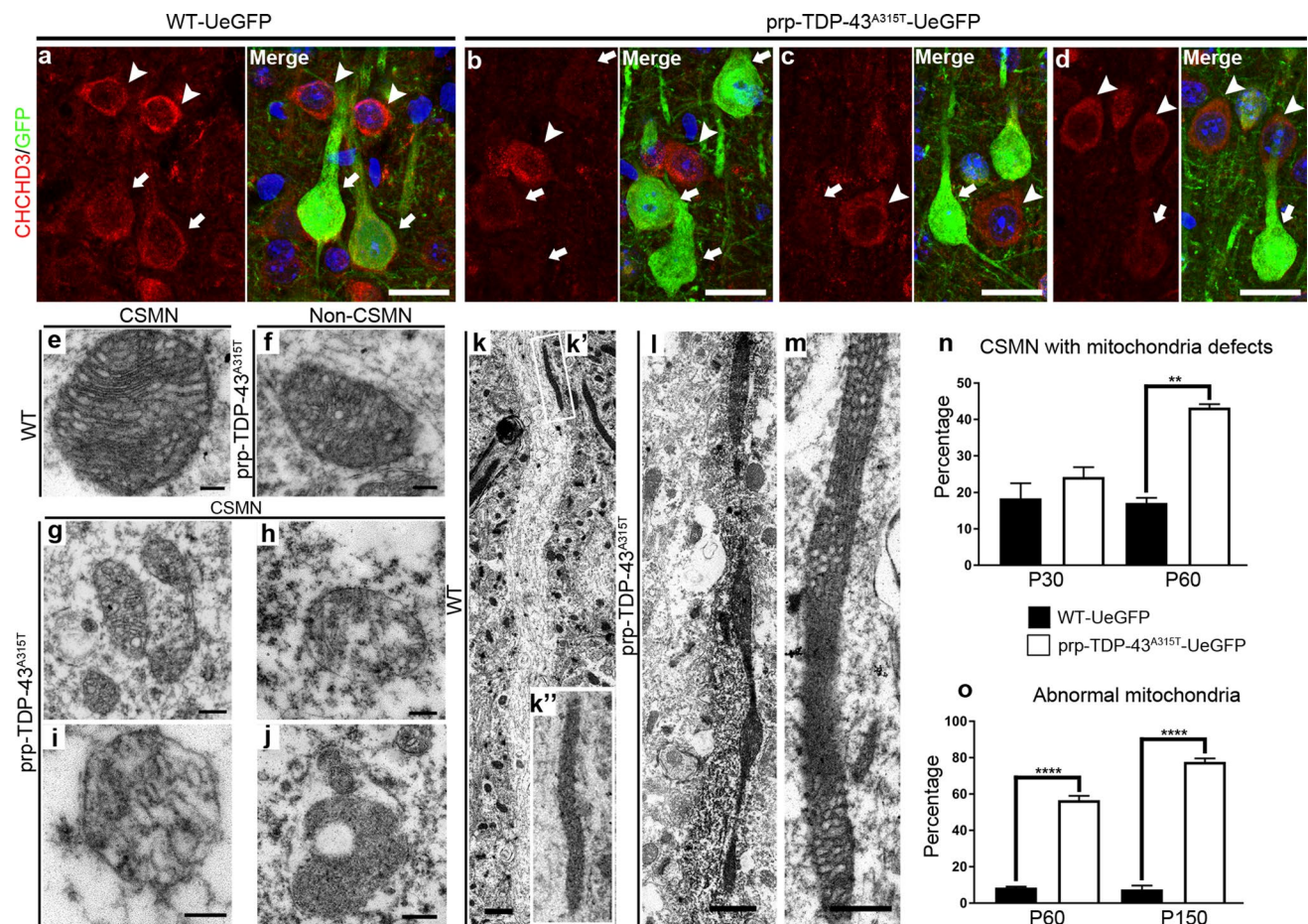


**Fig. 6** Mitochondrial defects in CSMN of prp-TDP-43<sup>A315T</sup> and prp-TDP-43<sup>A315T</sup>-UeGFP mice. **a–d** Representative images of CHCHD3 expression in WT-UeGFP and prp-TDP-43<sup>A315T</sup>-UeGFP mice (**b–d**) depicting loss of inner membrane in diseased CSMN (arrows) and normal levels in non-CSMN cells (arrowheads). Representative EM images of WT CSMN (**e**) and prp-TDP-43<sup>A315T</sup> non-CSMN (**f**) reveal normal mitochondrial morphology with intact inner membrane and cristae structure. In contrast, representative EM images in prp-TDP-43<sup>A315T</sup> CSMN reveal multiple mitochondrial defects including degeneration with reduced size (**g**), loss of their inner membrane (**h**), swollen and broken cristae structures (**i**), and engulfed mitochon-

dria by lysosomes (**j**). **k–k'** Representative EM images of normal mitochondria localized in the WT CSMN apical dendrite. **l, m** Representative EM images of mitochondria localized in the prp-TDP-43<sup>A315T</sup> CSMN apical dendrite revealing swelling intermittently and enlargement. **n–o** Quantitative analysis of percent CSMN that lack prominent CHCHD3 expression (**o**) Quantitative analysis of defective mitochondria in CSMN of WT-UeGFP and prp-TDP-43<sup>A315T</sup> at P60 and P150. Scale bars: **a–d** = 20 μm; **e–j** = 200 nm; **k, l** = 1 μm; **m** = 500 nm. Bar graphs represent mean ± SEM of at least three replicates. \*\* *p* < 0.01, \*\*\*\* *p* < 0.0001

with well-defined cristae and matrix (Fig. 6e). Likewise, non-CSMN cells in the motor cortex of prp-TDP-43<sup>A315T</sup> mice displayed healthy morphology (Fig. 6f). In striking contrast, mitochondria of prp-TDP-43<sup>A315T</sup> CSMN had numerous defects; they had broken cristae, swollen matrix, the integrity of their inner membrane was lost, and mitochondrial accumulations were fused with lysosomes (Fig. 6g–j).

The most remarkable defect was observed in the mitochondria in the apical dendrites. In WT CSMN, mitochondria can be detected along the apical dendrite (Fig. 6k, k' enlarged to the right bottom corner). However, in prp-TDP-43<sup>A315T</sup> CSMN, the mitochondria were extensively stretched and extended along the apical dendrite. Some even reached up to 12  $\mu\text{m}$  in length. These aberrantly long, defective mitochondria were present only in the CSMN of prp-TDP-43<sup>A315T</sup>-UeGFP mice (Fig. 6l, m), and had a “bead on a string” appearance, suggesting the presence of a mitochondrial fission problem.

EM analysis allowed us to assess health of mitochondria in detail. More than half of the mitochondria were defective in the CSMN of prp-TDP-43<sup>A315T</sup> mice by P60 (WT  $8.5 \pm 0.5\%$ ,  $n = 3$  mice; prp-TDP-43<sup>A315T</sup>  $56.3 \pm 2.3\%$ ,  $n = 3$  mice; ANOVA followed by Tukey's multiple comparison test, adjusted  $p$  value  $< 0.0001$ ; Fig. 6o) and by P150 among all mitochondria present inside diseased CSMN, a vast majority were without an intact inner membrane, or a proper cristae and were fused with a lysosome (WT  $7.5 \pm 2.1\%$ ,  $n = 3$  mice and prp-TDP-43<sup>A315T</sup>  $77.7 \pm 1.9\%$ ,  $n = 3$  mice; ANOVA followed by Tukey's multiple comparison test, adjusted  $p$  value  $< 0.0001$ ; Fig. 6o).

However, the health and integrity of mitochondria in non-CSMN did not differ between P60 (WT  $3.9 \pm 0.3\%$ ,  $n = 3$  mice and prp-TDP-43<sup>A315T</sup>  $4 \pm 0.7\%$ ,  $n = 3$  mice) and P150 (WT  $4.5 \pm 2.1\%$ ,  $n = 3$  mice and prp-TDP-43<sup>A315T</sup>  $4.8 \pm 1.6\%$ ,  $n = 3$  mice), suggesting the absence of age-related decline in mitochondrial health.

We next investigated whether mitochondrial defects observed in CSMN of prp-TDP-43<sup>A315T</sup>-UeGFP mice are recapitulated in the Betz cells of patients with TDP-43 pathology. Unlike CSMN of prp-TDP-43<sup>A315T</sup>-UeGFP mice, the differences between the healthy and diseased Betz cells were not as obvious with CHCHD3 expression profile (Fig. 7a–c). Human Betz cells were much larger than CSMN and they had many more CHCHD3 expression (observed as puncta) inside them. However, it was not possible to quantify mitochondrial health based on CHCHD3 expression, but the overall intensity of immunostaining called for a detailed EM analysis, which clearly distinguished healthy and diseased mitochondria. The mitochondria of Betz cells in control cases retained their structure and integrity (Fig. 7d). However, mitochondria in the Betz cells of ALS patients with TDP-43 pathology displayed a major defect (Fig. 7e–i);

even though the outer membrane remained intact, the inner membrane and the cristae were primarily disintegrated, generating a hollow and empty structure (healthy  $5.9 \pm 0.4\%$ ; defective  $94.1 \pm 0.4\%$ ;  $n = 3$  normal controls,  $n = 4$  patients; unpaired  $t$  test,  $p < 0.0001$ ; Fig. 7l). Other non-Betz cells located in close vicinity to Betz cells, however, had healthy mitochondria (healthy  $19 \pm 5.6\%$ ; defective  $81 \pm 5.6\%$ , unpaired  $t$  test,  $p < 0.0001$ ; Fig. 7j–k, m), suggesting that mitochondrial defects were mostly restricted to Betz cells in the motor cortex of ALS patients with TDP-43 pathology.

### Integrity of endoplasmic reticulum (ER)

Investigation of ER revealed yet another problem CSMN have in the presence of TDP-43 pathology. Calreticulin, which is expressed along the ER membrane, marks the location of the ER and suggests its integrity [42]. Calreticulin expression was detected in WT CSMN, like in other cells and neurons in the motor cortex (Fig. 8a), and its expression profile in CSMN of prp-TDP-43<sup>A315T</sup>-UeGFP mice (Fig. 8b, c) was decreased, justifying a detailed EM analysis. ER appeared normal with layers of cristae and ribosomes attached in healthy CSMN (Fig. 8d). However, in CSMN of prp-TDP-43<sup>A315T</sup>-UeGFP mice, the ER appeared vastly fragmented and did not have the normal stacked structure with defined cristae and lumen (Fig. 8e, f). The integrity of the ER was drastically compromised and at times small pieces of ER, either circular or in short fragmented lines with ribosomes attached, were detected in the cytoplasm.

We next asked whether these ER defects were also present in the Betz cells of patients with TDP-43 pathology. Betz cells were identified based on their location within layer 5 of the motor cortex, their pyramidal shape and large size, and high-level expression of Map2. Calreticulin expression was used to detect ER within Betz cells in both normal control and ALS with TDP-43 pathology cases (Fig. 9a–c). In striking contrast to normal controls, calreticulin expression revealed the presence of numerous ER with extensively enlarged size and shape (Fig. 9b, b', b'', c, c', c''); insets enlarged within the image) only in the Betz cells of ALS patients with TDP-43 pathology. These striking differences between healthy and diseased CSMN called for a detailed cellular analysis with EM. Betz cells ( $n = 32$ ) of normal control subjects ( $n = 3$ ) had very intricate and web-like ER, especially around the nucleus (Fig. 8d). However, the ER displayed a major pathology in the Betz cells of ALS patients ( $n = 52$  cells,  $n = 4$  patients) (Fig. 9e–h). Unlike the ER in the CSMN, these were not broken, but their lumens were extensively enlarged forming balloon-like structures. Some appeared as a “bead on a string”, and almost all were deformed. Regardless of their size and shape, the ribosomes were still attached but there were also numerous small pieces of ER with ribosomes

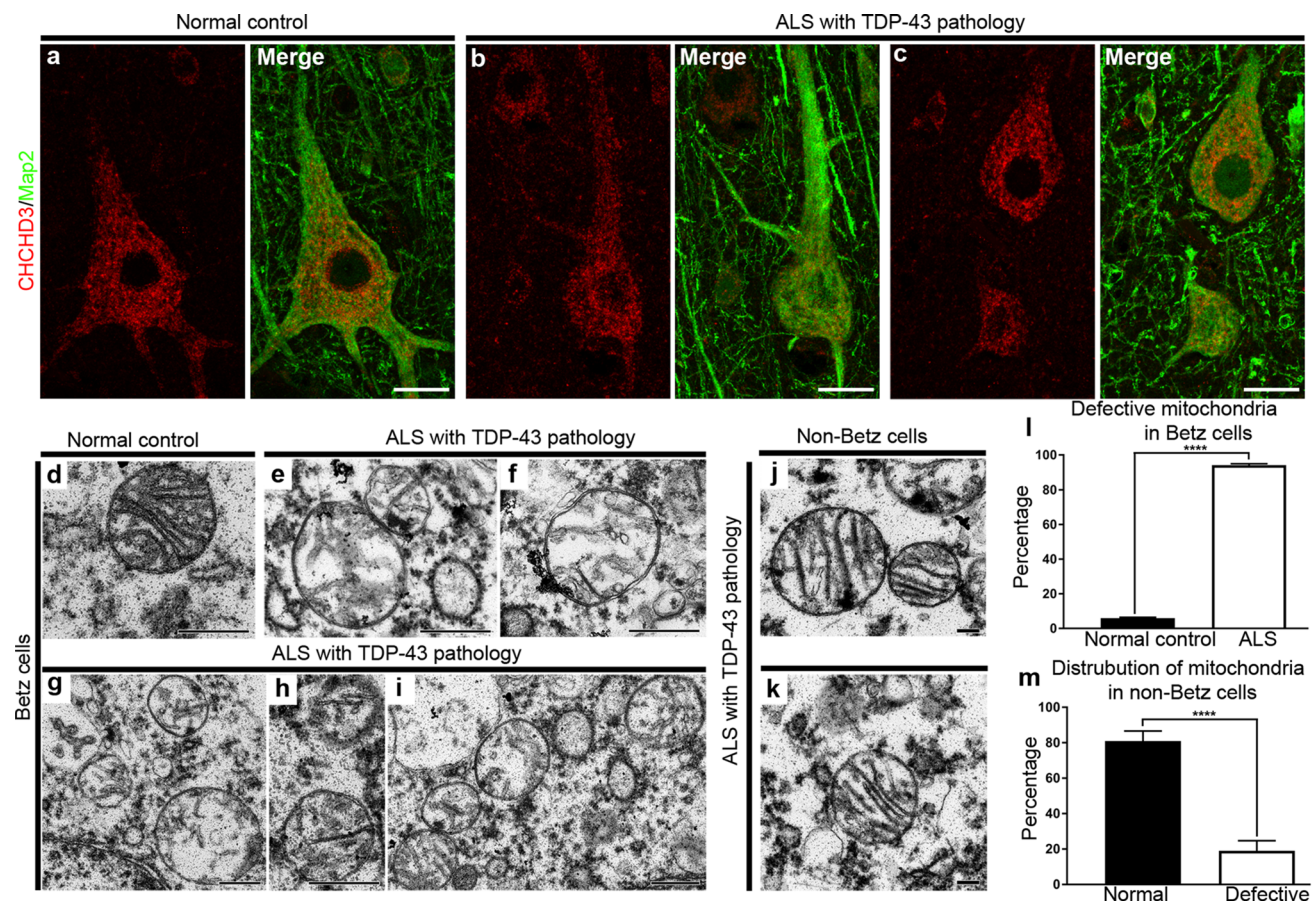


**Fig. 7** Mitochondria of Betz cells are selectively defective in ALS patients with TDP-43 pathology. Representative images of Betz cells expressing mitochondrial marker CHCHD3 and neuronal marker Map2 in normal controls (**a**) and ALS patients with TDP-43 pathology (**b–c**). **d** Representative EM image of healthy mitochondria in Betz cells of normal controls. **e–i** Representative EM images of mitochondria in Betz cells of ALS cases. **j–k** Representative EM images

of mitochondria in non-Betz cells. **l** Bar graph representing percentage of defective mitochondria in Betz cells of normal controls and ALS patients with TDP-43 pathology. **m** Bar graph representing percentage of defective mitochondria in non-Betz cells of normal controls and ALS cases. Scale bars: **a–c** = 20  $\mu$ m; **d–f** = 500 nm; **g–k** = 200 nm. Bar graphs represent mean  $\pm$  SEM of at least three replicates. \*\*\*\*  $p < 0.0001$

freely present in the cytosol. These extensively large ER were mostly accompanied with deformed mitochondria or lysosome.

We next investigated whether Betz cells that did not have TDP-43 inclusions in their cytoplasm and that were devoid of NCIs were also similarly affected in the motor cortex of ALS patients with TDP-43 pathology. TDP-43 and Map2 co-immuno marked Betz cells in the motor cortex and revealed their low levels of TDP-43 expression in the nucleus, without any cytoplasmic accumulations (Supplementary Fig. 2a, b), similar to Betz cells of control subjects (Fig. 2a–c, h). However, their EM analysis unraveled ultrastructural defects that occur in the nuclear membrane (Supplementary Fig. 2d), electron-dense cytoplasmic aggregates (Supplementary Fig. 2e), ER (Supplementary Fig. 2f) and mitochondria (Supplementary Fig. 2g), as observed in Betz cells with NCIs (Fig. 7, 8, 9). Even though the level and the extent of neuronal damage may vary, the underlying

pathology was common between Betz cells in the motor cortex of ALS patients with TDP-43 pathology.

We were intrigued by the presence of extensive cellular organelle defects in CSMN as early as P60, and that nuclear membrane, ER and the mitochondria all display ultrastructural defects, suggesting functional abnormalities. Then asked whether any of these problems in specific organelles occurred prior to others, and investigated the health and the integrity of the nuclear membrane, ER and the mitochondria at P15, a very early stage in the life of the prp-TDP-43<sup>A315T</sup> mice, when they are still with their moms in the nest, eyes just opening, and display no symptoms. The cyto-architecture of nuclear membrane, ER and the mitochondria all appeared normal and healthy in WT CSMN at P15 (Fig. 10a). Surprisingly, however, initial stages of structural defects were detected in the nuclear membrane, where some segments of the membrane were either convoluted inside the nucleus or towards the cytoplasm (Fig. 10b,

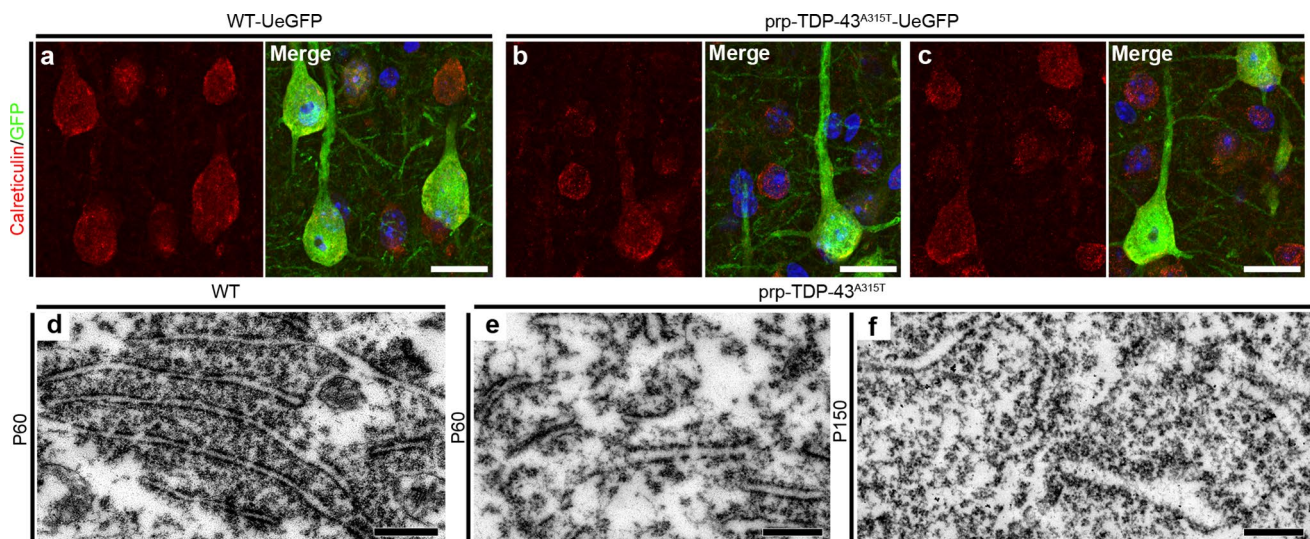


**Fig. 8** Endoplasmic reticulum integrity is disrupted in CSMN of prp-TDP-43<sup>A315T</sup> and prp-TDP-43<sup>A315T</sup>-UeGFP mice. Representative images showing CSMN expression of ER-lumen resident protein calreticulin in WT-UeGFP (a) and prp-TDP-43<sup>A315T</sup>-UeGFP mice

(b–c). Representative EM images of ER analysis in WT CSMN (d) and in prp-TDP-43<sup>A315T</sup> CSMN at P60 and P150 (e–f). Scale bars: a–c = 20  $\mu$ m; d–f = 1  $\mu$ m. Data shown are representative of at least three independent experiments

c), and albeit most of the ER appeared normal and healthy, some sections of the ER were found to be disintegrated and broken (Fig. 10d, e). Similarly, there were mitochondrial defects detected in CSMN of prp-TDP-43<sup>A315T</sup> mice as early as P15 (Fig. 10f, g). Some mitochondria had swollen and broken cristae in the CSMN of prp-TDP-43<sup>A315T</sup> mice and these were not present in the CSMN of WT mice. Their presence suggested that ultrastructural defects began to occur very early in the upper motor neurons, and they all occurred at similar times and rates in the nuclear membrane, ER and the mitochondria. Based on our findings, it was not possible to suggest that one of the ultrastructural defects preceded others, but rather they all began to occur very early and simultaneously in the upper motor neurons.

## Discussion

Upper motor neurons (UMN) are functionally and clinically important neuron populations that degenerate in ALS [16, 29] and related motor neuron diseases [17, 20]. It has long been thought that the UMN loss is a late event in the disease and a mere consequence of spinal motor neuron death and corticospinal tract degeneration. Thus, their contribution to disease progression has been widely questioned and they have not been acknowledged as a potential cellular target for therapeutic interventions. Only recently, numerous independent studies have begun to highlight early signs of their degeneration and dysfunction in ALS patients [22, 23, 69] and in different mouse models of the disease [21, 33, 47], revealing their early cellular degeneration and direct

involvement in disease pathology. Therefore, understanding the underlying causes of their vulnerability and progressive degeneration is paramount and extremely relevant for building effective treatment strategies.

TDP-43<sup>+</sup> protein aggregation is a hallmark of neurodegeneration, and this TDP-43 proteinopathy has been one of the most prominent pathologies observed in a broad spectrum of ALS and FTLN patients [40, 44, 60]. pTDP-43 is detected in the nucleus and its leakage to the cytoplasm, and subsequent accumulation there, is considered fundamental to TDP-43 pathology. Mutations in the *TARDBP* gene were also found to be linked and associated with TDP-43 pathology in patients with *TARDBP*-related ALS, which mainly serve the basis of generating mouse models that mimic human condition with mutations. Therefore, TDP-43 pathology has been studied at many different levels in many different diseases, and it is important to understand how neurons, especially the neurons that display early vulnerability in ALS, respond in the presence of TDP-43 mediated pathology.

Numerous studies already shed light on the normal function of TDP-43, and the underlying cellular events that are affected either when mutations in TDP-43 occur or when TDP-43<sup>+</sup> protein aggregates are present. However, none of these studies have assessed the health and the function of the UMN. This has been a demanding task for many reasons. The heterogeneity and the complexity of the cerebral cortex does not allow investigation of a distinct neuron population with cellular precision, and development of mouse model with an upper motor neuron phenotype is challenging. Here we overcame two important



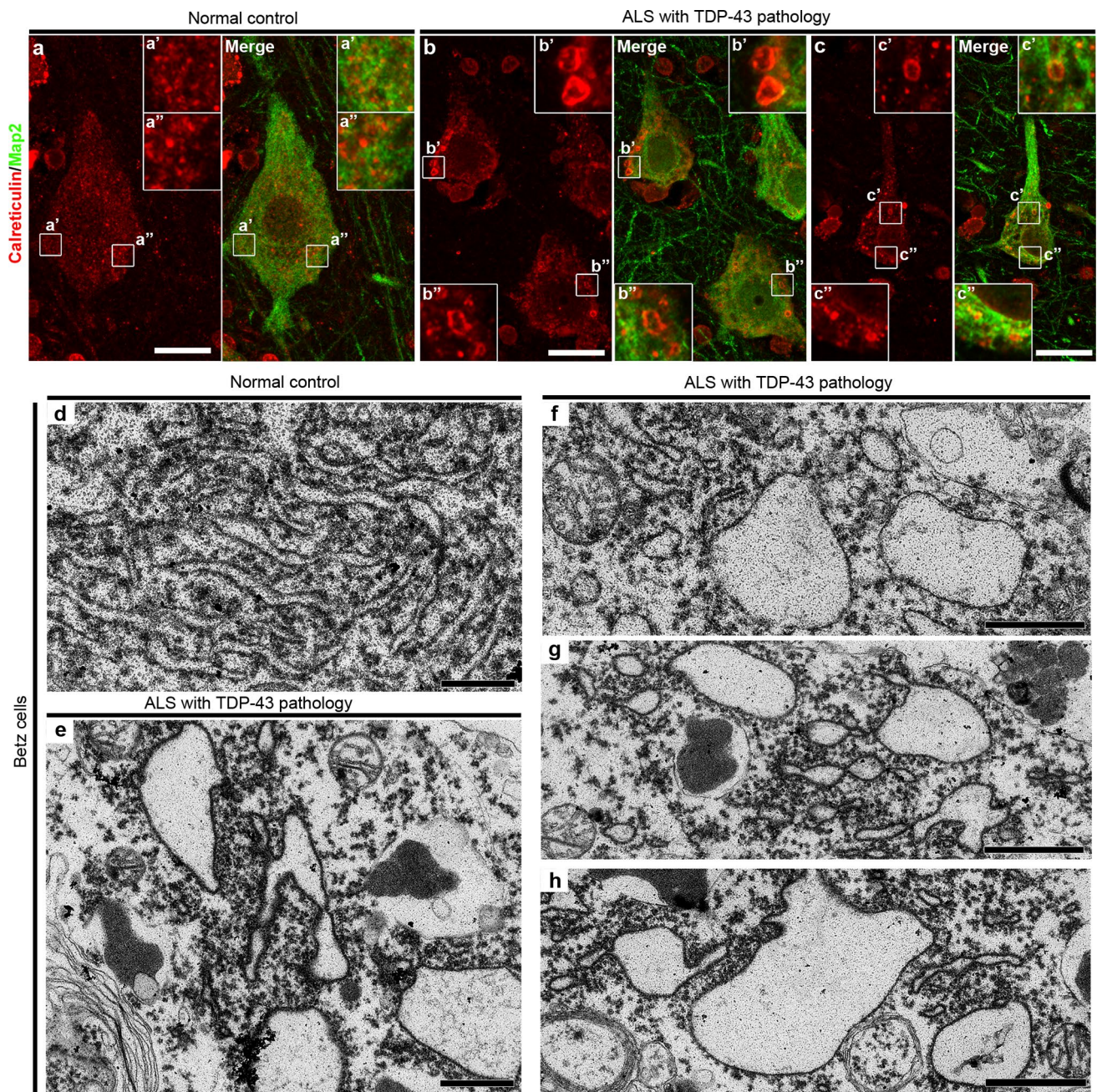


**Fig. 9** Endoplasmic reticulum of Betz cells with TDP-43 pathology displays massive ultrastructural defects. **a–c** Representative images showing Betz cells expressing ER-lumen resident protein calreticulin and neuronal marker Map2, showing evenly distributed ER in normal controls (**a, a''**), and distended and enlarged structures in ALS cases

(**b–b''**, **c–c''**). **d–h** Representative EM images of ER reveal that ER with cisternae are arranged in normal pattern in Betz cells of normal controls (**d**) and profoundly expanded in Betz cells of ALS cases (**e–h**). Scale bar: **a–c''** = 20  $\mu\text{m}$ ; **e–h** = 1  $\mu\text{m}$

limitations and began to shed light on the upper motor neurons that become diseased due to TDP-43 pathology, revealing novel cellular events that are perturbed in these neurons, as well as cellular defects that could be targets for drug treatment strategies in the near future. First, we studied the timing and the extent of CSMN degeneration in prp-TDP-43<sup>A315T</sup> mice, and since this mouse model of

TDP-43 displays progressive CSMN loss, we generated its CSMN reporter line using the UCHL1-eGFP mice, in which CSMN are genetically labeled with eGFP expression [76]. This allowed visualization and identification of CSMN among many different neurons and cells in the motor cortex and enabled precise cellular investigations of CSMN.

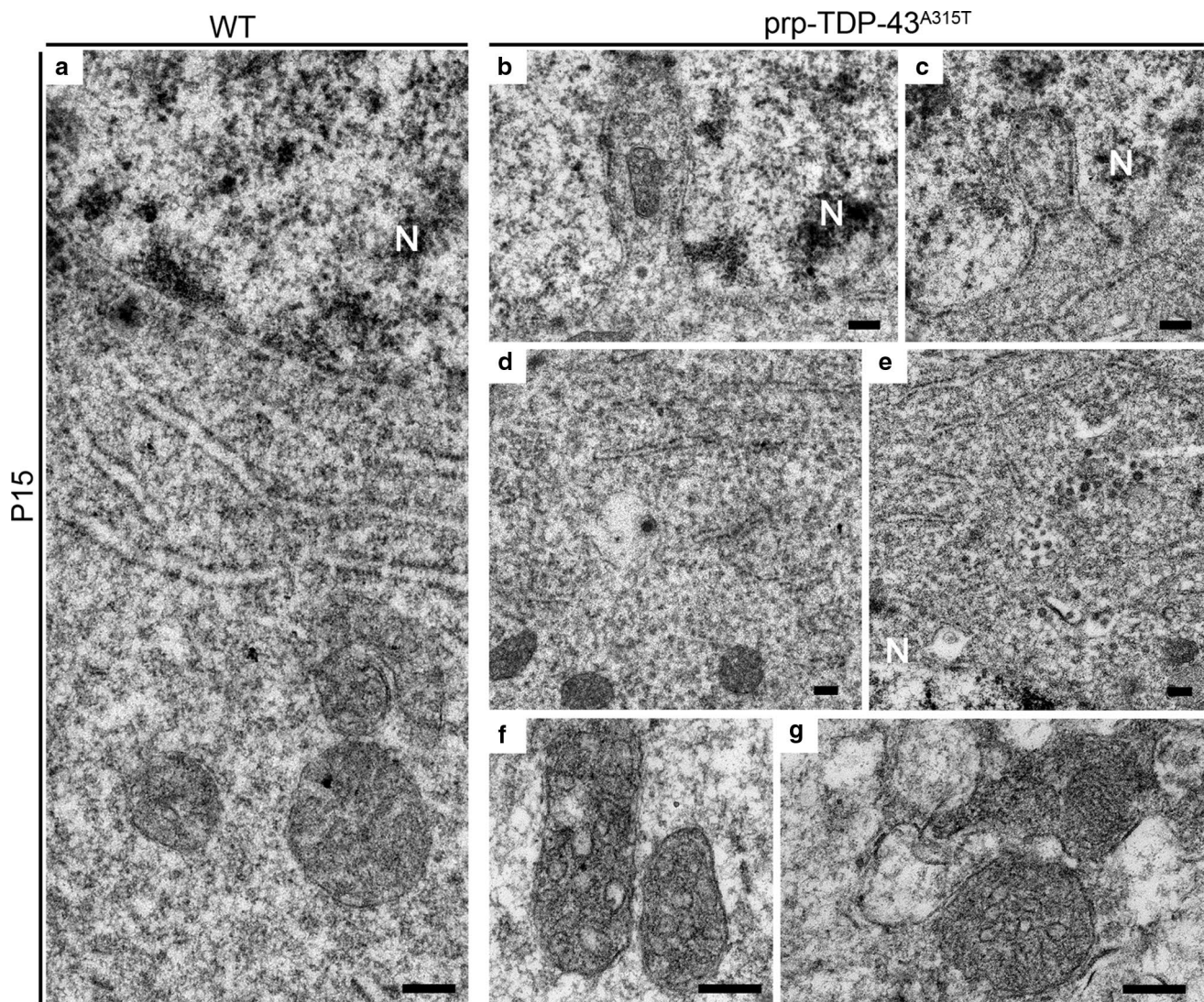


**Fig. 10** TDP-43 mutation renders cellular defects in CSMN as early as P15. **a** Representative electron microscopic view of Ctip2-labeled CSMN has normal nucleus, endoplasmic reticulum, and mitochondria. **b–g** However, CSMN of prp-TDP-43<sup>A315T</sup> mice display early

signs of nuclear membrane defects (**b–c**), ER disintegration (**d, e**), and mitochondrial defects (**f, g**) at this early age. N= nucleus Scale bar: 200 nm

Utilization of mouse models to understand diseases that affect motor neuron circuitry has been frustrating, because most of the mouse models generated based on single mutations detected in human patients do not display motor function defects. Therefore, many in the field suggest that mouse studies are not translational [39, 50]. However, we would like to propose a different explanation; the lack of translation is not because mice are not good disease models, but because we have been performing comparison at a species level, and not at a cellular level. When comparisons are made between the Betz cells and CSMN, we suggest that findings will be translational. In fact, here we find that upper motor neurons in two different species develop the same cellular defects with respect to TDP-43 pathology. Even the precise aspects

of their organelle-based pathologies are the same: both have defects in their nuclear membrane, mitochondria and ER. When the focus is shifted from mice to neuron, and when the cell biology of vulnerable and degenerating neurons is investigated in a cell-type specific manner with precision and detail, the basis of vulnerability and the underlying causes of cellular pathology will be revealed. Our results represent a manifestation of this argument.

Defects in nucleo-cytoplasmic shuttling of macromolecules have been suggested as a major phenomenon in ALS [35]. TDP-43 aggregates were found to sequester proteins involved in nuclear import of proteins and nuclear export of RNA, causing major imbalance in nucleo-cytoplasmic transport of biomolecules [13]. EM analysis of Betz cells

revealed how the cytoplasmic face of the nuclear membrane was extended to generate large pockets and how accumulations were detected mainly on the nuclear face of the membrane, suggesting a resistance for the directional flow from nucleus to cytoplasm. In addition, the formation of excessive kinks and groves along the nuclear membrane suggest that the Betz cells try to increase the surface area of the nuclear membrane to overcome potential nucleo-cytoplasmic transport defects. Even though TDP-43 pathology is widespread in the Betz cells of motor cortex, non-Betz cells do not appear to be under the same level and extent of pressure. It is important to note that due to prolonged hypoxia most patients experience peri-mortem, especially the cells and neurons that are sensitive to hypoxic insult, will be affected more than others. This may in part contribute to the ultrastructural damaged observed especially in the Betz cells of ALS patients, since these neurons are sensitive to hypoxic insult and are primarily involved with disease pathology in ALS. However, Betz cells of control cases, which were exposed to the same levels of hypoxia during postmortem interval (PMI), did not display similar pathologies, suggesting extensive ultrastructural defects observed in TDP-43 cases may not be solely explained by peri-mortem hypoxic insult.

Similar to Betz cells, we observed nuclear defects in CSMN of TDP-43 mouse model. Apart from morphological defects observed in the nucleus of diseased CSMN, molecules involved in nucleo-cytoplasmic transport such as RanGap1 and Transportin 1 were found to be dysregulated. Disruption of nucleo-cytoplasmic transport is an important component of ALS pathogenesis [77]. RanGap1 is one of the core molecules that regulate nucleocytoplasmic transport [49]. TDP-43 directly regulates RanGap1 and depletion of TDP-43 results in downregulation of RanGap1 [71]. Transportin 1 does not directly bind to TDP-43 [45] but TDP-43 aggregates sequester Transportin 1 in the cytoplasm of cortical neurons contributing to nucleo-cytoplasmic transport defects [13]. It has also been suggested that depletion of TDP-43 results in elevated levels of Transportin 1 [63]. Thus, our results suggest that nucleo-cytoplasmic transport is an important contributing factor in CSMN degeneration due to TDP-43 dysregulation.

Mitochondria, one of the most important organelles of the cell, play important roles in energy production, phospholipid biosynthesis, calcium homeostasis, and control over apoptosis [62]. It is no surprise that many of the genes that are linked to or associated with ALS code for proteins that are involved in mitochondrial function, and mitochondrial defects are accepted to be one of the converging neuronal problems detected in many different neurodegenerative diseases [19]. Morphologically abnormal mitochondria have been previously reported in many different mouse models of ALS [41, 70, 74], and presynaptic terminals of Betz cells

[56], but the defects we observe in the upper motor neurons with TDP-43 pathology are different. Here we find that mitochondria fail to retain inner membrane integrity, albeit the outer membrane remains intact. This suggests potential problems with ATP production in the Betz cells, as mitochondria require the inner membrane to generate the  $H^+$  gradient for ATP production. TDP-43 was shown to disrupt the contact point between mitochondria and ER, which is reported to be important especially for lipid biosynthesis and transport to mitochondria [65]. Upper motor neurons with TDP-43 pathology also lack proper contact of mitochondria with ER, which potentially exacerbates the cellular burden for ATP. It is also important to note that mitochondria along the apical dendrites of CSMN were extensively enlarged and this was only observed in diseased CSMN. Apical dendrites are active sites of neuronal communication and thus the energy demand is very high. The presence of such long and deformed mitochondria may suggest that the neuron is trying to compensate by increasing the size. Alternatively, there could be mitochondrial fission problems, which do not allow proper division of mitochondria to occur along the apical dendrites.

Endoplasmic reticulum (ER) is the site of protein synthesis. Defects in ER translate into problems with protein production, folding, and results in ER stress, one of the major common leading causes of neuronal vulnerability and degeneration [28, 59]. Alterations in ER morphology have been previously observed in spinal motor neurons of ALS mouse models and sporadic ALS patients [46, 55]. However, none of the findings reported such extensive ER defects Betz cells display in the presence of TDP-43 pathology. We find a profound increase in the size and the extent of the lumen of the ER, breaking, forming small circles, and disintegration. Interestingly, this pathology is conserved between mice and human and upper motor neurons in both species display major ER defects. Such profound defects suggest that the rate of protein production, and proper folding could be impaired in the upper motor neurons. Increased ER stress was reported to be an underlying cause for CSMN vulnerability [33], and ER stress has been detected in spinal motor neurons of many different disease models [3, 46, 55, 57, 68]. Here we show, for the first time, the extent of ER defects observed especially in the Betz cells of ALS patients with TDP-43 pathology.

The interaction site for ER and mitochondria recently gained attention for numerous cellular events [48], such as coordination of calcium transfer [52], regulation of mitochondrial fission [37], formation of membranes of autophagy [26], and initiation of inflammasomes [78]. Disruption of mitochondria-ER associated membranes (MAMs) resulted in disrupted lipid metabolism [27], calcium homeostasis [52], axonal transport [58], and increased autophagosome [26]. Since Betz cells of patients with TDP-43 pathology and

CSMN of *prp-TDP-43<sup>A315T</sup>* mice both displayed defects in their ER and mitochondria, it is very much possible that the cellular events that require their proper interaction will also be affected. Interestingly, TDP-43 was previously reported to modulate the ER–mitochondria interaction in both cell lines and in the spinal cord, by disrupting the VAPB–PTPIP51 interactions. Therefore, mutations in TDP-43 gene and protein accumulations containing TDP-43 may converge on cellular events that perturb MAMs, affecting numerous cellular events simultaneously.

Even though numerous similarities are observed between Betz cells of a broad spectrum of ALS patients with TDP-43 pathology and CSMN of a well-characterized mouse model for TDP-43, it is also important to mention subtle differences. For example, even though the ER was affected in both upper motor neurons, the extensive enlargement of the ER was not observed in CSMN, but the ER was disintegrated and mostly broken. Likewise, the enlargement of the space between the two lipid bi-layers of the nuclear membrane was observed only on the Betz cells of ALS patients, but the CSMN did not display such ultrastructural defects. However, the nuclear membrane of CSMN was also affected and the nuclear transport was impaired. The mouse model was generated based on the *A315T* mutation detected on the *TARDBP* gene of patients, and thus represents a genetic model of the disease, without major TDP-43 accumulations. In contrast, the patients included in this study were identified based on a pathological examination, and the presence of TDP-43 pathology in their motor cortex, but their genetic mutations were unknown, and most were sporadic. In addition, the Betz cells in patients and CSMN in mice differ in their projection field and connectivity with spinal cord targets. Therefore, in reality, the mouse and the human cases were representing two different spectrums of TDP-43 pathology. We think it is even more remarkable to find that despite species differences and the basis of developing TDP-43 pathology differing so strikingly, the similarities are astounding.

In conclusion, Betz cells of ALS patients with TDP-43 pathology have numerous cellular defects, especially with their nuclear membrane, mitochondria and ER. Interestingly, CSMN of *prp-TDP-43<sup>A315T</sup>* mice recapitulate ultrastructural defects observed in Betz cells of patients (Fig. 11). These defects begin to emerge as early as P15 in CSMN, suggesting their contribution to upper motor neuron vulnerability and progressive degeneration with respect to TDP-43 pathology. The close correlation between the Betz cells and CSMN provides a unique opportunity to reveal the underlying causes of upper motor neuron vulnerability, by focusing on the biology of CSMN at different stages of the disease using molecular and genetic approaches. Therefore, we would like to suggest that if we shift our focus to the cells and the neurons that become vulnerable in diseases, and take a look inside

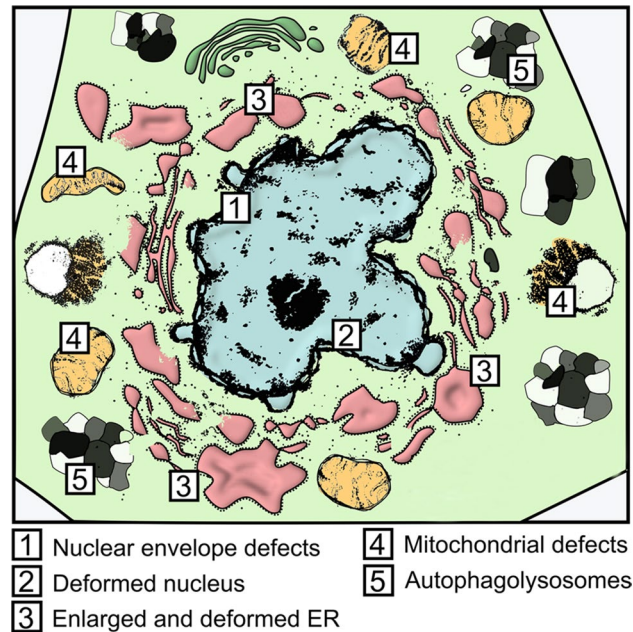


**Fig. 11** Schematic representation of intracellular defects observed in both Betz cells of ALS patients with TDP-43 pathology and CSMN of *prp-TDP-43<sup>A315T</sup>* mice

the vulnerable neurons to understand the very basis of their cellular problems, we may begin to reveal the causes of their vulnerability and the mode of their progressive degeneration. This information will help identify novel drug targets and will enable developing effective treatment strategies for numerous neurodegenerative diseases.

**Acknowledgements** This work was supported by NIH (R21NS085750, R01 NS085161) and Les Turner ALS Foundation. We thank Dr. Marco Martina and Gabriella Sekerkova for help with EM analysis, and Megan Schultz for immunohistochemistry experiments. We thank Jayson Wilson for excellent help with preparing sections of postmortem human samples.

**Author contributions** MG, JHJ, EHB, PHO designed the experiments. MG, JHJ, LER, NK, KDK conducted the experiments. MG, JHJ, EHB and PHO analyzed the data and wrote the manuscript.

## References

- Amador-Ortiz C, Lin WL, Ahmed Z, Personett D, Davies P, Duara R et al (2007) TDP-43 immunoreactivity in hippocampal sclerosis and Alzheimer's disease. *Ann Neurol* 61:435–445. <https://doi.org/10.1002/ana.21154>
- Arnold ES, Ling SC, Huelga SC, Lagier-Tourenne C, Polymenidou M, Ditsworth D et al (2013) ALS-linked TDP-43 mutations produce aberrant RNA splicing and adult-onset motor neuron disease without aggregation or loss of nuclear TDP-43. *Proc Natl Acad Sci U S A* 110:E736–E745. <https://doi.org/10.1073/pnas.1222809110>

3. Atkin JD, Farg MA, Walker AK, McLean C, Tomas D, Horne MK (2008) Endoplasmic reticulum stress and induction of the unfolded protein response in human sporadic amyotrophic lateral sclerosis. *Neurobiol Dis* 30:400–407. <https://doi.org/10.1016/j.nbd.2008.02.009>
4. Ayala YM, Zago P, D'Ambrogio A, Xu YF, Petrucelli L, Buratti E et al (2008) Structural determinants of the cellular localization and shuttling of TDP-43. *J Cell Sci* 121:3778–3785. <https://doi.org/10.1242/jcs.038950>
5. Bennett CL, Dastidar SG, Ling SC, Malik B, Ashe T, Wadhwa M et al (2018) Senataxin mutations elicit motor neuron degeneration phenotypes and yield TDP-43 mislocalization in ALS4 mice and human patients. *Acta Neuropathol*. <https://doi.org/10.1007/s00401-018-1852-9>
6. Bose JK, Huang CC, Shen CK (2011) Regulation of autophagy by neuropathological protein TDP-43. *J Biol Chem* 286:44441–44448. <https://doi.org/10.1074/jbc.M111.237115>
7. Braak H, Ludolph AC, Neumann M, Ravits J, Del Tredici K (2017) Pathological TDP-43 changes in Betz cells differ from those in bulbar and spinal alpha-motoneurons in sporadic amyotrophic lateral sclerosis. *Acta Neuropathol* 133:79–90. <https://doi.org/10.1007/s00401-016-1633-2>
8. Buratti E (2015) Functional significance of TDP-43 mutations in disease. *Adv Genet* 91:1–53. <https://doi.org/10.1016/bs.adgen.2015.07.001>
9. Buratti E, Baralle FE (2001) Characterization and functional implications of the RNA binding properties of nuclear factor TDP-43, a novel splicing regulator of CFTR exon 9. *J Biol Chem* 276:36337–36343. <https://doi.org/10.1074/jbc.M104236200>
10. Buratti E, Baralle FE (2008) Multiple roles of TDP-43 in gene expression, splicing regulation, and human disease. *Front Biosci* 13:867–878
11. Cannon A, Yang B, Knight J, Farnham IM, Zhang Y, Wuertzer CA et al (2012) Neuronal sensitivity to TDP-43 overexpression is dependent on timing of induction. *Acta Neuropathol* 123:807–823. <https://doi.org/10.1007/s00401-012-0979-3>
12. Chaudhury A, Chander P, Howe PH (2010) Heterogeneous nuclear ribonucleoproteins (hnRNPs) in cellular processes: focus on hnRNP E1's multifunctional regulatory roles. *RNA* 16:1449–1462. <https://doi.org/10.1261/rna.2254110>
13. Chou CC, Zhang Y, Umoh ME, Vaughan SW, Lorenzini I, Liu F et al (2018) TDP-43 pathology disrupts nuclear pore complexes and nucleocytoplasmic transport in ALS/FTD. *Nat Neurosci* 21:228–239. <https://doi.org/10.1038/s41593-017-0047-3>
14. Cykowski MD, Powell SZ, Peterson LE, Appel JW, Rivera AL, Takei H et al (2017) Clinical significance of TDP-43 neuropathology in amyotrophic lateral sclerosis. *J Neuropathol Exp Neurol* 76:402–413. <https://doi.org/10.1093/jnen/nlx025>
15. Darshi M, Mendiola VL, Mackey MR, Murphy AN, Koller A, Perkins GA et al (2011) ChChd3, an inner mitochondrial membrane protein, is essential for maintaining crista integrity and mitochondrial function. *J Biol Chem* 286:2918–2932. <https://doi.org/10.1074/jbc.M110.171975>
16. Eisen A, Pant B, Stewart H (1993) Cortical excitability in amyotrophic lateral sclerosis: a clue to pathogenesis. *Can J Neurol Sci* 20:11–16
17. Eymard-Pierre E, Lesca G, Dollet S, Santorelli FM, di Capua M, Bertini E et al (2002) Infantile-onset ascending hereditary spastic paralysis is associated with mutations in the alsin gene. *Am J Hum Genet* 71:518–527. <https://doi.org/10.1086/342359>
18. Fil D, DeLoach A, Yadav S, Alkam D, MacNicol M, Singh A et al (2017) Mutant Profilin1 transgenic mice recapitulate cardinal features of motor neuron disease. *Hum Mol Genet* 26:686–701. <https://doi.org/10.1093/hmg/ddw429>
19. Filosto M, Scarpelli M, Cotelli MS, Vielmi V, Todeschini A, Gregorelli V et al (2011) The role of mitochondria in neurodegenerative diseases. *J Neurol* 258:1763–1774. <https://doi.org/10.1007/s00415-011-6104-z>
20. Fink JK (2002) Hereditary spastic paraplegia. *Neurol Clin* 20:711–726
21. Gautam M, Jara JH, Sekerkova G, Yasvoina MV, Martina M, Ozdinler PH (2016) Absence of alsin function leads to corticospinal motor neuron vulnerability via novel disease mechanisms. *Hum Mol Genet* 25:1074–1087. <https://doi.org/10.1093/hmg/ddv631>
22. Geevasinga N, Menon P, Nicholson GA, Ng K, Howells J, Kril JJ et al (2015) Cortical function in asymptomatic carriers and patients with C9orf72 amyotrophic lateral sclerosis. *JAMA Neurol* 72:1268–1274. <https://doi.org/10.1001/jamaneurol.2015.1872>
23. Geevasinga N, Menon P, Ozdinler PH, Kiernan MC, Vucic S (2016) Pathophysiological and diagnostic implications of cortical dysfunction in ALS. *Nat Rev Neurol* 12:651–661. <https://doi.org/10.1038/nrneurol.2016.140>
24. Goossens J, Vanmechelen E, Trojanowski JQ, Lee VM, Van Broeckhoven C, van der Zee J et al (2015) TDP-43 as a possible biomarker for frontotemporal lobar degeneration: a systematic review of existing antibodies. *Acta Neuropathol Commun* 3:15. <https://doi.org/10.1186/s40478-015-0195-1>
25. Gurney ME, Pu H, Chiu AY, Dal Canto MC, Polchow CY, Alexander DD et al (1994) Motor neuron degeneration in mice that express a human Cu, Zn superoxide dismutase mutation. *Science* 264:1772–1775
26. Hamasaki M, Furuta N, Matsuda A, Nezu A, Yamamoto A, Fujita N et al (2013) Autophagosomes form at ER-mitochondria contact sites. *Nature* 495:389–393. <https://doi.org/10.1038/nature11910>
27. Helle SC, Kanfer G, Kolar K, Lang A, Michel AH, Kornmann B (2013) Organization and function of membrane contact sites. *Biochim Biophys Acta* 1833:2526–2541. <https://doi.org/10.1016/j.bbamcr.2013.01.028>
28. Hetz C, Saxena S (2017) ER stress and the unfolded protein response in neurodegeneration. *Nat Rev Neurol* 13:477–491. <https://doi.org/10.1038/nrneurol.2017.99>
29. Huynh W, Simon NG, Grosskreutz J, Turner MR, Vucic S, Kiernan MC (2016) Assessment of the upper motor neuron in amyotrophic lateral sclerosis. *Clin Neurophysiol* 127:2643–2660. <https://doi.org/10.1016/j.clinph.2016.04.025>
30. Igaz LM, Kwong LK, Lee EB, Chen-Plotkin A, Swanson E, Unger T et al (2011) Dysregulation of the ALS-associated gene TDP-43 leads to neuronal death and degeneration in mice. *J Clin Invest* 121:726–738. <https://doi.org/10.1172/JCI44867>
31. Izumikawa K, Nobe Y, Yoshikawa H, Ishikawa H, Miura Y, Nakayama H et al (2017) TDP-43 stabilises the processing intermediates of mitochondrial transcripts. *Sci Rep* 7:7709. <https://doi.org/10.1038/s41598-017-06953-y>
32. Janssens J, Wils H, Kleinberger G, Joris G, Cuijt I, Ceuterick-de Groote C et al (2013) Overexpression of ALS-associated p.M337 V human TDP-43 in mice worsens disease features compared to wild-type human TDP-43 mice. *Mol Neurobiol* 48:22–35. <https://doi.org/10.1007/s12035-013-8427-5>
33. Jara JH, Genc B, Cox GA, Bohn MC, Roos RP, Macklis JD et al (2015) Corticospinal motor neurons are susceptible to increased ER stress and display profound degeneration in the absence of UCHL1 function. *Cereb Cortex* 25:4259–4272. <https://doi.org/10.1093/cercor/bhu318>
34. Jara JH, Genc B, Klessner JL, Ozdinler PH (2014) Retrograde labeling, transduction, and genetic targeting allow cellular analysis of corticospinal motor neurons: implications in health and disease. *Front Neuroanat* 8:16. <https://doi.org/10.3389/fnana.2014.00016>
35. Kim HJ, Taylor JP (2017) Lost in transportation: nucleocytoplasmic transport defects in ALS and other neurodegenerative diseases. *Neuron* 96:285–297. <https://doi.org/10.1016/j.neuron.2017.07.029>

36. Kinoshita Y, Ito H, Hirano A, Fujita K, Wate R, Nakamura M et al (2009) Nuclear contour irregularity and abnormal transporter protein distribution in anterior horn cells in amyotrophic lateral sclerosis. *J Neuropathol Exp Neurol* 68:1184–1192. <https://doi.org/10.1097/NEN.0b013e3181bc3bec>
37. Korobova F, Ramabhadran V, Higgs HN (2013) An actin-dependent step in mitochondrial fission mediated by the ER-associated formin INF2. *Science* 339:464–467. <https://doi.org/10.1126/science.1228360>
38. Ling SC, Polymenidou M, Cleveland DW (2013) Converging mechanisms in ALS and FTD: disrupted RNA and protein homeostasis. *Neuron* 79:416–438. <https://doi.org/10.1016/j.neuron.2013.07.033>
39. Ludolph AC, Bendotti C, Blaugrund E, Chio A, Greensmith L, Loeffler JP et al (2010) Guidelines for preclinical animal research in ALS/MND: a consensus meeting. *Amyotroph Lateral Scler* 11:38–45. <https://doi.org/10.3109/17482960903545334>
40. Mackenzie IR, Bigio EH, Ince PG, Geser F, Neumann M, Cairns NJ et al (2007) Pathological TDP-43 distinguishes sporadic amyotrophic lateral sclerosis from amyotrophic lateral sclerosis with SOD1 mutations. *Ann Neurol* 61:427–434. <https://doi.org/10.1002/ana.21147>
41. Magrane J, Cortez C, Gan WB, Manfredi G (2014) Abnormal mitochondrial transport and morphology are common pathological denominators in SOD1 and TDP43 ALS mouse models. *Hum Mol Genet* 23:1413–1424. <https://doi.org/10.1093/hmg/ddt528>
42. Muller-Taubenberger A, Lupas AN, Li H, Ecker M, Simmeth E, Gerisch G (2001) Calreticulin and calnexin in the endoplasmic reticulum are important for phagocytosis. *EMBO J* 20:6772–6782. <https://doi.org/10.1093/emboj/20.23.6772>
43. Nakashima-Yasuda H, Uryu K, Robinson J, Xie SX, Hurtig H, Duda JE et al (2007) Co-morbidity of TDP-43 proteinopathy in Lewy body related diseases. *Acta Neuropathol* 114:221–229. <https://doi.org/10.1007/s00401-007-0261-2>
44. Neumann M, Sampathu DM, Kwong LK, Truax AC, Micsenyi MC, Chou TT et al (2006) Ubiquitinated TDP-43 in frontotemporal lobar degeneration and amyotrophic lateral sclerosis. *Science* 314:130–133. <https://doi.org/10.1126/science.1134108>
45. Nishimura AL, Zupunski V, Troakes C, Kathe C, Fratta P, Howell M et al (2010) Nuclear import impairment causes cytoplasmic trans-activation response DNA-binding protein accumulation and is associated with frontotemporal lobar degeneration. *Brain* 133:1763–1771. <https://doi.org/10.1093/brain/awq111>
46. Oyanagi K, Yamazaki M, Takahashi H, Watabe K, Wada M, Komori T et al (2008) Spinal anterior horn cells in sporadic amyotrophic lateral sclerosis show ribosomal detachment from, and cisternal distention of the rough endoplasmic reticulum. *Neuropathol Appl Neurobiol* 34:650–658. <https://doi.org/10.1111/j.1365-2990.2008.00941.x>
47. Ozdinler PH, Bann S, Yamamoto TH, Guzel M, Brown RH Jr, Macklis JD (2011) Corticospinal motor neurons and related subcerebral projection neurons undergo early and specific neurodegeneration in hSOD1G(9)(3)A transgenic ALS mice. *J Neurosci* 31:4166–4177. <https://doi.org/10.1523/JNEUROSCI.4184-10.2011>
48. Paillusson S, Stoica R, Gomez-Suaga P, Lau DHW, Mueller S, Miller T et al (2016) There's something wrong with my MAM; the ER-mitochondria axis and neurodegenerative diseases. *Trends Neurosci* 39:146–157. <https://doi.org/10.1016/j.tins.2016.01.008>
49. Pemberton LF, Paschal BM (2005) Mechanisms of receptor-mediated nuclear import and nuclear export. *Traffic* 6:187–198. <https://doi.org/10.1111/j.1600-0854.2005.00270.x>
50. Picher-Martel V, Valdmanis PN, Gould PV, Julien JP, Dupre N (2016) From animal models to human disease: a genetic approach for personalized medicine in ALS. *Acta Neuropathol Commun* 4:70. <https://doi.org/10.1186/s40478-016-0340-5>
51. Pinarbasi ES, Cagatay T, Fung HYJ, Li YC, Chook YM, Thomas PJ (2018) Active nuclear import and passive nuclear export are the primary determinants of TDP-43 localization. *Sci Rep* 8:7083. <https://doi.org/10.1038/s41598-018-25008-4>
52. Rowland AA, Voeltz GK (2012) Endoplasmic reticulum-mitochondria contacts: function of the junction. *Nat Rev Mol Cell Biol* 13:607–625. <https://doi.org/10.1038/nrm3440>
53. Ruffoli R, Bartalucci A, Frati A, Fornai F (2015) Ultrastructural studies of ALS mitochondria connect altered function and permeability with defects of mitophagy and mitochondriogenesis. *Front Cell Neurosci* 9:341. <https://doi.org/10.3389/fncel.2015.00341>
54. Saberi S, Stauffer JE, Jiang J, Garcia SD, Taylor AE, Schulte D et al (2018) Sense-encoded poly-GR dipeptide repeat proteins correlate to neurodegeneration and uniquely co-localize with TDP-43 in dendrites of repeat-expanded C9orf72 amyotrophic lateral sclerosis. *Acta Neuropathol* 135:459–474. <https://doi.org/10.1007/s00401-017-1793-8>
55. Sasaki S (2010) Endoplasmic reticulum stress in motor neurons of the spinal cord in sporadic amyotrophic lateral sclerosis. *J Neuropathol Exp Neurol* 69:346–355. <https://doi.org/10.1097/NEN.0b013e3181d44992>
56. Sasaki S, Iwata M (1999) Ultrastructural change of synapses of Betz cells in patients with amyotrophic lateral sclerosis. *Neurosci Lett* 268:29–32
57. Saxena S, Cabuy E, Caroni P (2009) A role for motoneuron subtype-selective ER stress in disease manifestations of FALS mice. *Nat Neurosci* 12:627–636. <https://doi.org/10.1038/nn.2297>
58. Saxton WM, Hollenbeck PJ (2012) The axonal transport of mitochondria. *J Cell Sci* 125:2095–2104. <https://doi.org/10.1242/jcs.053850>
59. Schroder M, Kaufman RJ (2005) ER stress and the unfolded protein response. *Mutat Res* 569:29–63. <https://doi.org/10.1016/j.mrfmmm.2004.06.056>
60. Scotter EL, Chen HJ, Shaw CE (2015) TDP-43 proteinopathy and ALS: insights into disease mechanisms and therapeutic targets. *Neurotherapeutics* 12:352–363. <https://doi.org/10.1007/s13311-015-0338-x>
61. Shan X, Chiang PM, Price DL, Wong PC (2010) Altered distributions of Gemini of coiled bodies and mitochondria in motor neurons of TDP-43 transgenic mice. *Proc Natl Acad Sci U S A* 107:16325–16330. <https://doi.org/10.1073/pnas.1003459107>
62. Smith EF, Shaw PJ, De Vos KJ (2017) The role of mitochondria in amyotrophic lateral sclerosis. *Neurosci Lett*. <https://doi.org/10.1016/j.neulet.2017.06.052>
63. Stalekar M, Yin X, Rebolj K, Darovic S, Troakes C, Mayr M et al (2015) Proteomic analyses reveal that loss of TDP-43 affects RNA processing and intracellular transport. *Neuroscience* 293:157–170. <https://doi.org/10.1016/j.neuroscience.2015.02.046>
64. Stallings NR, Puttaparthi K, Luther CM, Burns DK, Elliott JL (2010) Progressive motor weakness in transgenic mice expressing human TDP-43. *Neurobiol Dis* 40:404–414. <https://doi.org/10.1016/j.nbd.2010.06.017>
65. Stoica R, De Vos KJ, Paillusson S, Mueller S, Sancho RM, Lau KF et al (2014) ER-mitochondria associations are regulated by the VAPB-PTPIP51 interaction and are disrupted by ALS/FTD-associated TDP-43. *Nat Commun* 5:3996. <https://doi.org/10.1038/ncomms4996>
66. Swarup V, Phaneuf D, Bareil C, Robertson J, Rouleau GA, Kriz J et al (2011) Pathological hallmarks of amyotrophic lateral sclerosis/frontotemporal lobar degeneration in transgenic mice produced with TDP-43 genomic fragments. *Brain* 134:2610–2626. <https://doi.org/10.1093/brain/awr159>
67. Torres P, Ramirez-Nunez O, Romero-Guevara R, Bares G, Granada-Serrano AB, Ayala V et al (2018) Cryptic exon splicing function of tdrbp interacts with autophagy in nervous tissue. *Autophagy*. <https://doi.org/10.1080/15548627.2018.1474311>

68. Vijayalakshmi K, Alladi PA, Ghosh S, Prasanna VK, Sagar BC, Nalini A et al (2011) Evidence of endoplasmic reticular stress in the spinal motor neurons exposed to CSF from sporadic amyotrophic lateral sclerosis patients. *Neurobiol Dis* 41:695–705. <https://doi.org/10.1016/j.nbd.2010.12.005>
69. Vucic S, Kiernan MC (2006) Novel threshold tracking techniques suggest that cortical hyperexcitability is an early feature of motor neuron disease. *Brain* 129:2436–2446. <https://doi.org/10.1093/brain/awl172>
70. Wang W, Li L, Lin WL, Dickson DW, Petrucelli L, Zhang T et al (2013) The ALS disease-associated mutant TDP-43 impairs mitochondrial dynamics and function in motor neurons. *Hum Mol Genet* 22:4706–4719. <https://doi.org/10.1093/hmg/ddt319>
71. Ward ME, Taubes A, Chen R, Miller BL, Sephton CF, Gelfand JM et al (2014) Early retinal neurodegeneration and impaired Ran-mediated nuclear import of TDP-43 in progranulin-deficient FTL. *J Exp Med* 211:1937–1945. <https://doi.org/10.1084/jem.20140214>
72. Wegorzewska I, Bell S, Cairns NJ, Miller TM, Baloh RH (2009) TDP-43 mutant transgenic mice develop features of ALS and frontotemporal lobar degeneration. *Proc Natl Acad Sci U S A* 106:18809–18814. <https://doi.org/10.1073/pnas.0908767106>
73. Wils H, Kleinberger G, Janssens J, Pereson S, Joris G, Cuijt I et al (2010) TDP-43 transgenic mice develop spastic paralysis and neuronal inclusions characteristic of ALS and frontotemporal lobar degeneration. *Proc Natl Acad Sci U S A* 107:3858–3863. <https://doi.org/10.1073/pnas.0912417107>
74. Xu YF, Gendron TF, Zhang YJ, Lin WL, D'Alton S, Sheng H et al (2010) Wild-type human TDP-43 expression causes TDP-43 phosphorylation, mitochondrial aggregation, motor deficits, and early mortality in transgenic mice. *J Neurosci* 30:10851–10859. <https://doi.org/10.1523/JNEUROSCI.1630-10.2010>
75. Xu YF, Zhang YJ, Lin WL, Cao X, Stetler C, Dickson DW et al (2011) Expression of mutant TDP-43 induces neuronal dysfunction in transgenic mice. *Mol Neurodegener* 6:73. <https://doi.org/10.1186/1750-1326-6-73>
76. Yasvoina MV, Genc B, Jara JH, Sheets PL, Quinlan KA, Milosevic A et al (2013) eGFP expression under UCHL1 promoter genetically labels corticospinal motor neurons and a subpopulation of degeneration-resistant spinal motor neurons in an ALS mouse model. *J Neurosci* 33:7890–7904. <https://doi.org/10.1523/JNEUROSCI.2787-12.2013>
77. Zhang K, Donnelly CJ, Haeusler AR, Grima JC, Machamer JB, Steinwald P et al (2015) The C9orf72 repeat expansion disrupts nucleocytoplasmic transport. *Nature* 525:56–61. <https://doi.org/10.1038/nature14973>
78. Zhou R, Yazdi AS, Menu P, Tschopp J (2011) A role for mitochondria in NLRP3 inflammasome activation. *Nature* 469:221–225. <https://doi.org/10.1038/nature09663>